



Coupling Phenomena in Magnetocaloric Materials

Anja Waske,^[a, d] Biswanath Dutta,^[b] Niclas Teichert,^[c] Bruno Weise,^[a] Navid Shayanfar,^[b] Andreas Becker,^[c] Andreas Hütten,^{*, [c]} and Tilmann Hickel^[b]

Strong coupling effects in magnetocaloric materials are the key factor to achieve a large magnetic entropy change. Combining insights from experiments and ab initio calculations, we review relevant coupling phenomena, including atomic coupling, stress coupling, and magnetostatic coupling. For the investigations on atomic coupling, we have used Heusler compounds as a flexible model system. Stress coupling occurs in first-order magnetocaloric materials, which exhibit

a structural transformation or volume change together with the magnetic transition. Magnetostatic coupling has been experimentally demonstrated in magnetocaloric particles and fragment ensembles. Based on the achieved insights, we have demonstrated that the materials properties can be tailored to achieve optimized magnetocaloric performance for cooling applications.

1. Introduction

The prospect of efficient solid-state refrigeration at room temperature has led to a large interest in materials showing a magnetocaloric effect (MCE).^[1] Compared to conventional vapor-cycle refrigeration, solid-state cooling shows many advantages. Firstly, potentially hazardous refrigerants are obsolete and secondly the potential system efficiency improves. Materials exhibiting an MCE can be divided into two classes: second-order magnetocaloric materials show a conventional magnetic transition such as, for example, the ferro- to paramagnetic transition in elemental gadolinium.^[2] In first-order magnetocaloric materials, the magnetic phase transition occurs jointly with a change in the structure of the material, leading to “giant” magnetocaloric effects as observed in, for example, $\text{Gd}_5\text{Si}_2\text{Ge}_2$,^[1] La–Fe–Si-based^[3] and Mn–Fe–P-based alloys,^[4] and NiMn-based Heusler compounds.^[5] The magnetostructural transitions governing first-order magnetocaloric materials show that strong coupling phenomena occur in this material class. In fact, many of the characteristics of these materials can be understood by an investigation of their coupling effects. In this Review, a wide definition of the term “coupling” is used, that refers to any kind of interaction between neighboring atoms, grains, and even particles. Hereby, a scale-bridging understanding of the involved coupling phenomena and how they determine the functional properties of magnetocaloric materials is provided. The types of coupling covered in this Review with the corresponding section numbers are shown in Figure 1. Atomic coupling of magnetic and lattice degrees of freedom determines the adiabatic temperature change of the material in first-order magnetostructural transformations. Stress coupling of different variants or classes of MCE materials will occur at interfaces, which are in principle present in any realistic material system. During operation, MCE materials will experience substantial external magnetic fields and magnetic exchange fields, which will experience magnetostatic coupling across different regions of

the sample. Even when occurring individually, many of these mechanisms are not yet fully understood. The challenge of many MCE materials is, however, that these couplings occur simultaneously and influence each other. The intention of this review is therefore, to provide an overview of the scientific and technological aspects related to these coupling mechanisms based on Heusler compounds and $\text{La}(\text{Fe},\text{Si})_{13}$ as two of the most competitive magnetocaloric materials.

Although the majority of studies on magnetocaloric materials deal with polycrystalline bulk or ribbon samples, the interest in thin film materials is constantly growing. Thin films are not only conceivable for nanotechnological cooling devi-

[a] Dr. A. Waske, B. Weise
Institute for Complex Materials
IFW Dresden
Helmholtzstraße 20, 01069 Dresden (Germany)

[b] Dr. B. Dutta, N. Shayanfar, Dr. T. Hickel
Computational Materials Design
Max-Planck-Institut für Eisenforschung GmbH
Max-Planck-Straße 1, 40237 Düsseldorf (Germany)

[c] Dr. N. Teichert, A. Becker, Prof. Dr. A. Hütten
Department of Physics
Bielefeld University
Universitätsstr. 25, 33615 Bielefeld (Germany)
E-mail: huetten@physik.uni-bielefeld.de

[d] Dr. A. Waske
Bundesanstalt für Materialforschung und -prüfung (BAM)
Unter den Eichen 87, 12205 Berlin (Germany)

The ORCID identification number(s) for the author(s) of this article can be found under:
<https://doi.org/10.1002/ente.201800163>.

© 2018 The Authors. Published by Wiley-VCH Verlag GmbH & Co. KGaA. This is an open access article under the terms of the Creative Commons Attribution Non-Commercial License, which permits use, distribution and reproduction in any medium, provided the original work is properly cited, and is not used for commercial purposes.

This publication is part of a Special Issue on “Ferroic Cooling”. To view the complete issue, visit: <http://dx.doi.org/10.1002/ente.v6.8>.

ces but also allow for the simplification of materials engineering due to high throughput methods.^[6] Furthermore, epitaxial thin films grown on single-crystalline substrates serve as ideal model systems for structural characterization,^[7,8] and to uncover the role of interfaces between different magnetocaloric materials.^[9,10] For the consideration of various types of atomic coupling and coupling phenomena in thin films, Heusler compounds are the focus of this Review article due

to their diversity of mechanisms. Magnetostatic coupling and stress-coupling in bulk materials are dependent on, and especially relevant for, the operation and design of magnetocaloric regenerators. Because of this, we focused on highly technologically relevant La(Fe,Si)₁₃-based materials for the consideration of these coupling phenomena.

2. Coupling on the Atomic Scale

An understanding of the coupling between the magnetic and the structural degrees of freedom is of pivotal importance for the optimization of MCE materials. In many cases, the different magnetic states of the austenite and the martensite phases are exploited upon triggering the martensitic transition with a magnetic field. Moreover, many of the promising MCE materials undergo a coupled magnetostructural transition, as this yields the largest entropy or temperature changes. Such a coupling can be simulated phenomenologically at the mesoscale, by imposing certain interaction strengths. Buchelnikov et al.^[11] for example, have used a many-body Hamiltonian to study the combined transition in different magnetic Heusler compounds. The underlying physical mechanisms for the coupling of magnetic and lattice entropy, however, are determined by the individual atoms and their electrons. Therefore, first principles calculations provide the best chance to investigate and improve these mechanisms at the atomic scale.

Heusler compounds are promising candidates for magnetic refrigeration. Full Heusler compounds have the generic formula X₂YZ and crystallize at high temperatures in the L2₁ structure.^[12] The MCE for many Heusler materials occurs jointly with a structural transformation from the cubic L2₁ (or B2) austenite to a tetragonal or orthorhombic martensite (L1₀, 14M, 10M, 4O).^[13] Besides the fact that most Heusler systems consist only of common, rather inexpensive elements their major advantage is that temperature and hysteresis of the martensitic transformation (MT) can be tuned by adjusting their composition by thermo-chemical coupling.^[14] One important parameter characterizing the transformation temperature is the valence electron concentration per atom (*e/a*) which is determined by the chemical composition.

The Curie temperature of the austenite phase (*T_C*) is crucial for determining the temperature range in which the inverse MCE (iMCE) can proceed. The value of *T_C* can be tuned by substitution of a small amount of Ni by a fourth element, for example, Co.^[15,16] Co substitution is known not only for increasing the iMCE in Ni–Mn–X (X = In, Sn, Sb), but also for converting the MCE in Ni–Mn–Ga from a conventional (i.e., cMCE) to an inverse type in Ni–Co–Mn–Ga.^[17] Moreover, a partial Co substitution for Ni in weakly magnetocaloric Ni–Mn–Al alloys leads to an evolving iMCE in Ni–Co–Mn–Al^[18,19] due to chemo-magnetic coupling. Ni–Mn–Al shows weakly ferromagnetic or antiferromagnetic (B2) behavior in the austenite phase when crystallized in the L2₁ or B2 structure, respectively,^[20] and the corresponding 10M or 14M martensite phase exhibits antiferromagnetic coupling or spin-glass behavior.^[21] Co substitution for Ni

Dr. Anja Waske is group leader at the Leibniz Institute for Solid State and Materials Research (IFW) Dresden and head of the division "Radiological methods" at the Federal Institute for Materials Research and Testing, Berlin, Germany. She studied Physics at the Technische Universität Dresden, followed by a PhD thesis in the field of X-ray tomographic characterization of granular matter. Her research interests are magnetic composites and magnetocaloric materials for cooling and energy harvesting applications. Anja develops 3D image analysis methods for understanding the properties of functional and additively manufactured materials.



Andreas Hütten received his PhD in physics from Göttingen University in Germany and worked subsequently as a Feodor Lynen Research Fellow at UC Berkeley and Lawrence Berkeley National Laboratory in the U.S. After being staff researcher at the Leibniz Institute for Solid State and Materials Research at Dresden in Germany and at the Institute of Nanotechnology at the KIT Karlsruhe in Germany, he was appointed as Professor at the Department of Physics at Bielefeld University in Germany. His research is mainly devoted to the physics of thin films and nanostructures. He has published more than 200 articles in reputed journals and is serving as an editorial board member for Sensors.



Tilmann Hickel studied physics at Humboldt University Berlin, Germany, and Loughborough University, England, and finished his PhD in 2005 on many-body theories for magnetic materials. He afterwards joined the Max-Planck-Institut für Eisenforschung GmbH, where he became in 2006 head of the group "Computational Phase Studies" within the department "Computational Materials Design". His group focuses on *ab initio* simulation of materials properties and phase stabilities at finite temperatures. His interests cover structural materials such as steels as well as functional and, in particular, magnetocaloric materials.



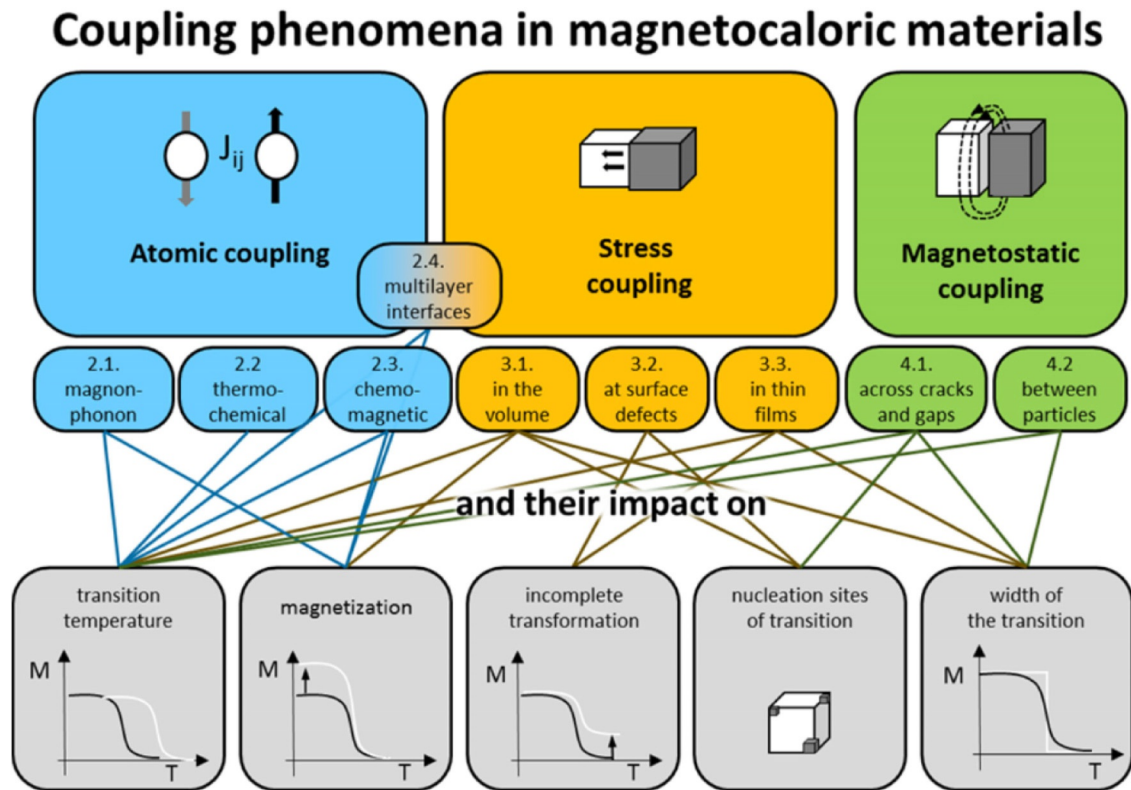


Figure 1. Schematic illustration of the coupling phenomena occurring in magnetocaloric materials and how they impact the functional properties.

leads to a substantial increase of the austenite magnetization and, hence, a remarkable magnetization difference ΔM between martensite and austenite that enables a giant inverse magnetocaloric effect.^[18,19]

2.1. Magnon–phonon coupling in stoichiometric phases

As one step in this direction, we have simulated the delicate interplay between the magnetic and the vibrational degrees of freedom when determining the martensitic transition temperature (T_M) in NiMn-based Heusler compounds. The *ab initio* total energies and the Hellmann–Feynman forces for this and most of the following investigations have been determined by employing density functional theory (DFT) as implemented in the plane-wave-based Vienna Ab initio Simulation Package (VASP).^[22] The application of the projector augmented wave (PAW) method,^[23] and the generalized gradient approximation (GGA) parameterized by Perdew–Burke–Ernzerhof (PBE)^[24] for the exchange–correlation functional has been proven to provide reliable results for NiMn-based Heusler systems. More technical details of the DFT calculations are presented in the referenced publications. To capture the finite temperature properties within the free energy of the involved phases, DFT energies at $T=0$ K need to be combined with thermodynamic concepts for the different entropy contributions.^[25]

First, *ab initio* calculations for the martensitic phase transition have been performed for the Heusler system

Ni_2MnGa .^[26] The corresponding free energy difference between the cubic austenite ($L2_1$) and the non-modulated tetragonal martensite ($L1_0$) phases is shown in Figure 2 (top panel). The main temperature dependence stems from lattice vibrations, for which the quasiharmonic approximation is sufficient in the present case. Considering solely this entropy contribution (blue dashed line), the calculated martensitic

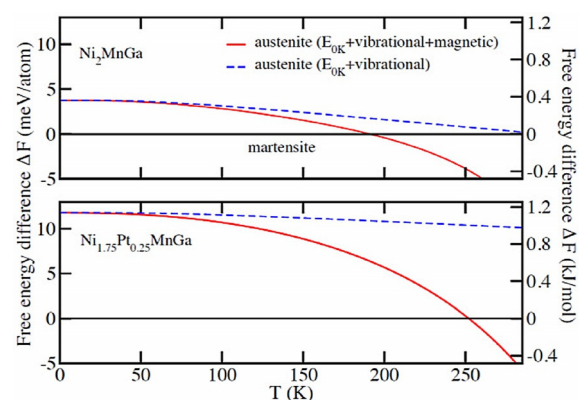


Figure 2. Calculated free energy difference ΔF between the austenite and the non-modulated martensite phases in Ni_2MnGa (upper panel) and $\text{Ni}_{1.75}\text{Pt}_{0.25}\text{MnGa}$ (lower panel). The pure contribution of lattice vibrations (blue dashed lines) is compared to calculations in which the impact of magnetic excitations on phonons is taken into account (red solid lines). A positive free energy difference indicates the stability of martensite, whereas the intersection with the zero line corresponds to the transition to the austenite phase.^[28]

transition temperature T_M , however, is overestimated by approximately 100 K as compared to the experimental value. Furthermore, imaginary phonons indicate that the structure is thermodynamically unstable.^[26] The coupling to the magnetic excitations needs to be taken into account to describe the mechanisms at the phase transition correctly. The main consequence of spin waves in Heusler systems such as Ni_2MnGa and Ni_2MnAl is the reduction of the local Ni moment.^[27] This can be considered with a fixed spin-moment (FSM) approach, in which the size of the magnetic moment in the DFT supercell is constrained such that the magnetization curve is correctly reproduced. The corresponding DFT calculation reduces the energy difference between the austenite and martensite. More importantly, it stabilizes the previously observed soft phonon mode. The consequence of such a treatment for the free energy difference (Figure 2, red solid line) is a change of T_M from above room temperature (without this consideration) to 182 K, which is in good agreement with the experimental value.

The validity of such an approach to the coupling of vibrational and magnetic degrees of freedom has meanwhile been demonstrated for several MCE Heusler systems. Particularly strong are the corrections if a small amount of Pt is alloyed to the otherwise stoichiometric Ni_2MnGa (Figure 2, bottom panel).^[28] In this case the vibrational entropy contributions alone would yield a T_M that is dramatically higher than in Ni_2MnGa , whereas the consideration of the coupling to magnetism yields only a moderate increase. The resulting change of the martensitic transition temperature to values close to room temperature for $\text{Ni}_{1.75}\text{Pt}_{0.25}\text{MnGa}$, has been quantitatively confirmed experimentally and makes the material system particularly interesting for applications.

Additional interesting findings in Pt-enriched $\text{Ni}_{1.9}\text{Pt}_{0.1}\text{MnGa}$ follow from synchrotron X-ray powder diffraction (SXRPD) measurements indicating a cubic premartensite to Bain-distorted premartensite transition at a temperature of approximately 235 K.^[29] Our first-principles calculations reveal that the coupling of chemistry to the volume expansion due to Pt substitution is responsible for the observed Bain distortion (Figure 3a). A similar effect of volume on the energy surface of the premartensite phase has afterwards been seen (even without Pt) in stoichiometric Ni_2MnGa (Figure 3b). The finite temperature coupling of the vibrational and magnetic degrees of freedom is again important in this case: a reduced magnetization at finite temperature captured through FSM calculations stabilizes the cubic premartensite phase (Figure 3b). Hence, though the Pt substitution at the Ni site modifies the energy plateau found for Ni_2MnGa through the enhanced volume and stabilizes the robust Bain-distorted premartensite phase at lower temperatures, the finite temperature decrease in magnetization will stabilize the cubic premartensite phase at higher temperatures. This explains the experimentally observed sequence of structural transitions in the premartensite phase.

One should note that the FSM approach only captures the coupling of lattice and magnetic degrees of freedom in Ni_2MnGa and $\text{Ni}_{2-x}\text{Pt}_x\text{MnGa}$ close to ferromagnetic saturation.

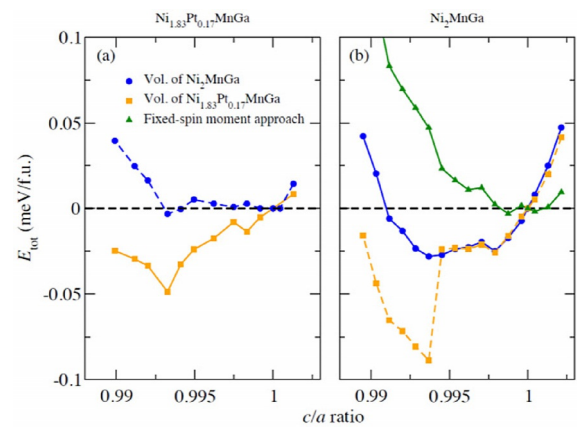


Figure 3. Variation of the total energy at $T=0$ K with the c/a ratio for the 3M premartensite phase of (a) $\text{Ni}_{1.83}\text{Pt}_{0.17}\text{MnGa}$ and (b) Ni_2MnGa . Square symbols correspond to calculations performed at the equilibrium volume of $\text{Ni}_{1.83}\text{Pt}_{0.17}\text{MnGa}$, whereas circles denote calculations performed at the equilibrium volume of Ni_2MnGa . The energy computed using a fixed-spin moment approach for Ni_2MnGa at the equilibrium volume of $\text{Ni}_{1.83}\text{Pt}_{0.17}\text{MnGa}$ is shown by triangles.^[29]

tion. However, for optimum magnetocaloric effects, strong magnetization changes in the relevant temperature range are desired. To understand the coupling in this case as well requires more sophisticated treatments.^[30–32] One important starting point in this direction is the paramagnetic high-temperature limit, where the local magnetic moments are fluctuating at a time scale that is much shorter than atomic motions. The coupling to the lattice vibrations is then best described if the atomic forces are averaged over all possible spin configurations. Such a spin-space average (SSA) explains, for example, the dynamic stability of face-centered cubic Fe at elevated temperatures.^[33] For many MCE materials, the transition from ferro- to paramagnetism also needs to be simulated. This can be achieved by considering a superposition of the two limiting cases:

$$F_j^{\text{SSA}}(T) \approx \alpha(T)F_j^{\text{FM}} + [1 - \alpha(T)]F_j^{\text{PM}}$$

Here, the coupling parameter $\alpha(T)$ is the temperature-dependent internal energy of the magnetic subsystem determined by numerically solving an effective nearest-neighbor Heisenberg model with quantum Monte Carlo simulations. In this way, one limits the direct calculation of atomic forces to the fully ordered (F_j^{FM}) and fully disordered (F_j^{PM}) magnetic configurations. The approach has been tested for body-centered cubic Fe, as this is the only system for which temperature-dependent experimental phonon energies are available across the ferro- to paramagnetic transition.^[34,35] The obtained results on the phonon dispersions and the phonon density-of-states are shown in Figure 4. It can be clearly seen that a good agreement with the experimental results for all temperatures, including those above T_c , can be achieved only with such a magnon–phonon coupling approach. This indicates that the magnetic short-range order is significant even considerably above T_c . The SSA approach has recently been extended to random solid solutions,^[31] to explain the unusual

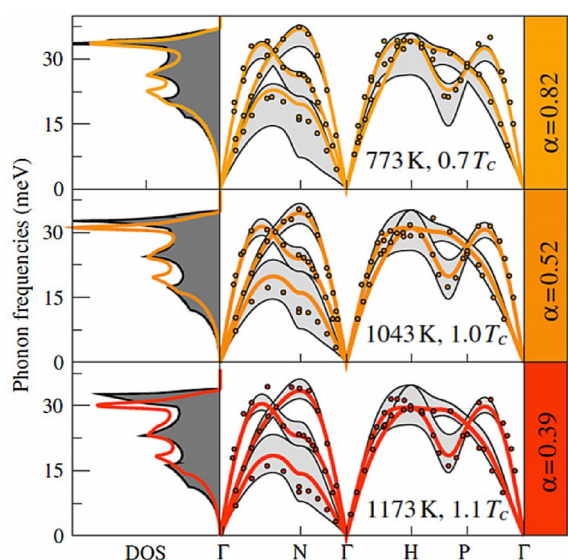


Figure 4. Phonon density-of-states (DOS) and phonon dispersion of bcc Fe at three different temperatures. Symbols indicate experimental data obtained by neutron scattering experiments.^[34] The light-gray shaded area within the phonon dispersion plots indicates the range between $\alpha = 1$ (FM limit) and $\alpha = 0$ (PM limit). The orange-to-red thick lines indicate the theoretical predictions for the corresponding α value (given to the right). The left panel shows the theoretical DOS (colored) and the DOS obtained by fitting the neutron spectra by a Born-von-Kármán fit^[35] (dark gray shaded area).^[30]

phonon hardening for some acoustic phonon modes in Fe–Pd and Fe–Pt as a function of temperature. Such a consideration of chemical disorder is also important for MCE materials of the Heusler type, as their optimum properties are usually observed for off-stoichiometric compositions (see Section 2.2).

A more complete description of the coupling of lattice and magnetic degrees of freedom is achieved if they are treated at comparable time scales.^[32,36] For example, molecular dynamics (MD) simulations of pure Fe have been performed in the paramagnetic state. After every five such MD steps, the magnetic configuration was modified, whereas the lattice degrees were frozen in at this moment.^[36] Based on this method, the impacts of the dynamics on the size of the magnetic moments and the electronic structure were investigated. In an even more advanced approach, the evolution of the spin system during the MD was described by spin dynamics.^[32] This study gave, for example, access to the destabilization of short-range-order spin configurations due to lattice vibrations by evaluating the spin autocorrelation function. Using such sophisticated approaches, the full information of the coupled structural–magnetic entropy change during martensitic phase transitions should, in principle, be accessible by computer simulations. However, the transfer of the methods from pure Fe to MCE materials of practical relevance is still beyond current capabilities of the employed methods.

2.2. Thermo-chemical coupling in off-stoichiometric Heusler compounds

Most of the promising magnetocaloric materials exhibit the largest MCE only at off-stoichiometric compositions. The un-

derstanding of the martensitic transformation at such compositions requires a proper treatment of the coupling between the chemical and the other thermodynamic (phonons, magnons) degrees of freedom. Extending the concepts developed for stoichiometric Ni_2MnGa further to the case of off-stoichiometric compositions, we have explored the Mn-rich part of the phase diagram (i.e., $\text{Ni}_2\text{Mn}_{1+y}\text{Ga}_{1-y}$).^[37] The Mn-rich off-stoichiometric composition has been achieved by considering one Mn antisite per supercell. To minimize the computational demand, the free energies at intermediate compositions have been determined from the interpolation of the calculated free energies at two different compositions (i.e., at stoichiometric and one off-stoichiometric composition). Figure 5 shows that the calculated martensitic transition temperature (T_M) increases monotonically with increasing Mn content. Near the stoichiometric composition, five-fold modulated martensite ($5M_C$) forms a phase boundary with the austenite ($L2_1$) whereas for larger Mn content, non-modulated $L1_0$ martensite is in direct contact with the austenite phase. The calculated T_M values show excellent agreement with the corresponding experimental results.^[37,38]

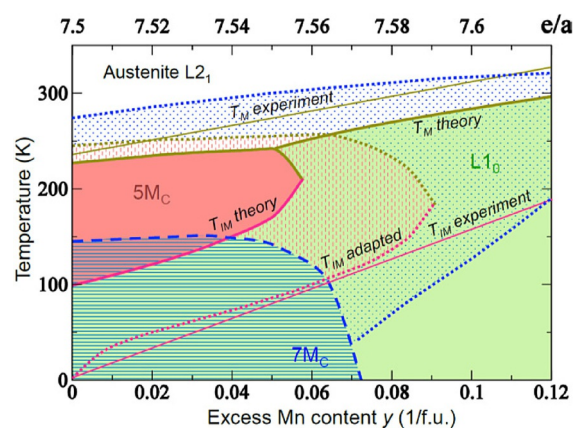


Figure 5. Ab initio calculated phase diagram of $\text{Ni}_2\text{Mn}_{1+y}\text{Ga}_{1-y}$. The martensitic transformation T_M (thick green line) separates the austenite ($L2_1$) from different martensitic phases ($L1_0$, $5M_C$, and $7M_C$). The intermartensitic transformation T_{IM} (thick red line) occurs between the $5M_C$ (red-colored area) and the $L1_0$ phase (green-colored area). The thin green and red lines show experimental T_M and T_{IM} . The red-textured area shows the extension of the $5M_C$ stability region, if its free energy at the stoichiometric composition is adapted to experimental data. The stability region of $7M_C$ is indicated by a blue dashed line with a numerical uncertainty given by blue dotted lines.^[37]

Determining the intermartensitic transition temperature is important for optimized MCE performance as the microstructure influences the materials stability and probably also the hysteresis of the martensitic transition.^[39] At the same time, the reliability of the experimental results for the intermartensitic transition is significantly lowered by the large hysteresis, whereas theoretically calculated stability regions depend sensitively on parameters such as the Curie temperature (T_C). As shown in Figure 5, the calculated $5M_C$ -to- $L1_0$ transition temperatures differ from the experimental results by about 100 K. However, an excellent agreement between the two can be achieved only by tuning the free energy of

the $5M_c$ phase by 1.13 meV per atom. The stability region of the $7M_c$ martensite is even more difficult to establish because of its structural similarity with the $L1_0$ martensite. Based on the choice of T_c , the stability of $7M_c$ martensite can show remarkable changes as demonstrated in Figure 5. A proper understanding and control of the intermartensitic transition can be an important step in the future designs of improved magnetocaloric materials, which has been shown recently in an experimental study.^[40]

A more complex chemical coupling with the vibrational and the magnetic degrees of freedom can happen in the chemically disordered B2 structure, which Heusler compounds show at higher temperature. For some Heusler compounds (e.g., Mn-rich Ni–Mn–Al alloys), the B2-to- $L2_1$ transition temperature is too low for any kind of atomic reordering to take place and hence the austenite phase in these alloys has the chemically disordered B2 structure. In a recent study, we have combined experimental and theoretical investigations to understand the impact of the chemical disorder on the martensitic transition and the magnetic properties, which are relevant for magnetocaloric applications.^[41]

2.3. Chemo-magnetic coupling in doped Heusler compounds

The near-room-temperature MT in Mn-rich Ni–Mn–Z (Z = Al, In, Sn, Sb) Heusler compounds is accompanied by a small change in magnetization and hence results in negligible MCE. Employing the strong chemo-magnetic coupling in these alloys, it is a common route to increase the magnetization change during MT and hence the MCE by doping the system with a small amount of Co or Fe.^[15,42] Previous experimental measurements showed that due to the substitution of Co or Fe for Ni, the magnetization of the high-temperature cubic austenite phase gets significantly enhanced, whereas the change for the low-temperature martensite phase is very minimal.^[42,43] Using ab initio calculations it has been shown that the addition of Co or Fe changes the magnetic state of the cubic austenite phase of $Ni_{50-x}M_xMn_{37.5}Al_{12.5}$ (M = Co or Fe).^[44] For the case of $Ni_{50}Mn_{37.5}Al_{12.5}$ the excess Mn atoms occupying the Al sub-lattice align in the opposite direction to the host Mn atoms, which is referred to as the AFM_E state. The substitution of Co or Fe however aligns all Mn spins irrespective of their occupation in the same direction and is referred to as the FM state. Figure 6 shows that the critical amount of Co needed for the AFM_E -to-FM transition is lower than that of Fe. This indicates that Co induces ferromagnetism more strongly than Fe, which is also supported by the magnetic exchange parameters. In $Ni_{50}Mn_{37.5}Al_{12.5}$, the Mn–Mn_{excess} antiferromagnetic interaction is the largest, which stabilizes the system in the AFM_E state (Figure 7a). The addition of Co and Fe changes the magnetic state because of their strong ferromagnetic interactions with the Mn atoms (Figure 7b). Although both the Co–Mn and the Fe–Mn interactions are ferromagnetic, the interaction strength of the Co–Mn pair is almost double than that of the Fe–Mn pair, which explains the lower critical amount of Co required for the AFM_E -to-FM transition. In the martensite phase, the

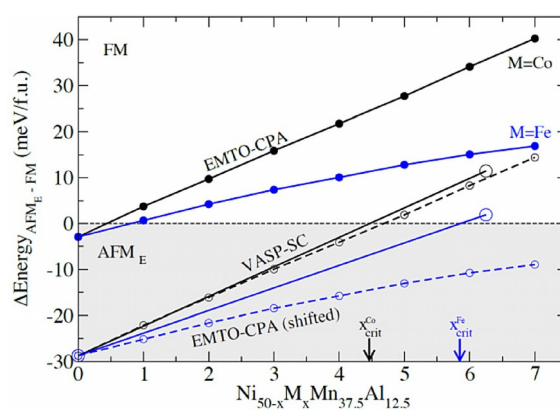


Figure 6. The difference of total energies between the AFM_E and the FM states as function of Co and Fe content in $Ni_{50-x}Co_xMn_{37.5}Al_{12.5}$ (black circles) and $Ni_{50-x}Fe_xMn_{37.5}Al_{12.5}$ (blue circles). The large open circles indicate results obtained using VASP whereas the smaller filled circles correspond to EMTO-CPA computed results. The EMTO-CPA (shifted) results denoted by smaller open circles refer to EMTO-CPA computed values after being shifted down by 26 meV per formula unit (f.u.) so that the result for $Ni_{50}Mn_{37.5}Al_{12.5}$ is aligned with the corresponding VASP computed value.^[44]

largest ferromagnetic interaction is however three times weaker than the Mn–Mn_{excess} antiferromagnetic interaction (Figure 7c,d). This explains the reason behind the unchanged magnetic state of the martensite phase even with Co or Fe doping.

The substitution of Co or Fe, however, can have a detrimental effect on the martensitic transition temperature. Firstly, no martensitic transition is possible in the FM state with the cubic austenite phase being stable for the entire energy surface. A tetragonal ground-state structure indicating a stable martensite can be observed in the AFM_E state (Figure 8). The energy difference between cubic austenite ($c/a=1$) and tetragonal martensite ($c/a>1.25$) in the AFM_E state however gets reduced due the addition of both Co and Fe. An approximate evaluation of the martensitic transition temperature based on the ground-state energy difference between the cubic austenite and the tetragonal martensite indicates that the substitution of Fe lowers the transition temperature more severely than that of Co.

Hence, the substitution of Co on the one hand improves the ferromagnetic properties of the austenite more significantly, whereas, on the other hand, it reduces the martensitic transformation temperature less severely. A combination of these two aspects makes Co-substituted Ni–Mn–Z Heusler compounds promising candidates for future magnetocaloric applications.

Furthermore, the impact of chemical doping on the magnetocrystalline anisotropy energy (MAE) has been investigated. Being the driving force for the rearrangement of martensitic variants under an applied magnetic field, the MAE can provide important information on the magnetic-field-induced strain in ferromagnetic shape memory alloys.^[45] Recent investigations have even observed a large influence of magnetocrystalline anisotropy on the MCE with a significant difference in the adiabatic temperature change and the

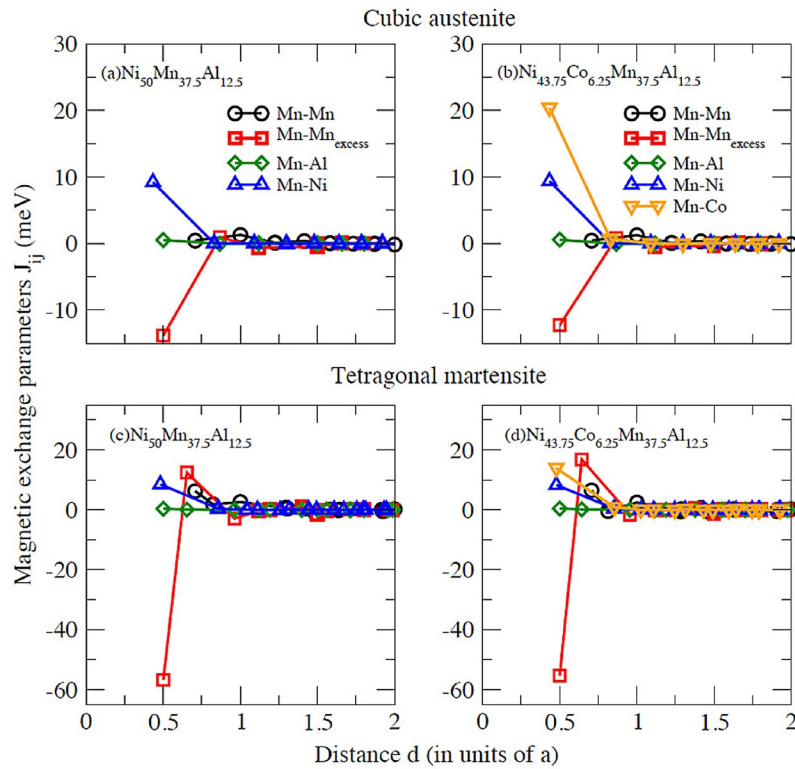


Figure 7. Calculated magnetic exchange parameters as a function of distance between the host Mn and the rest of the atoms in units of the lattice constant a for cubic austenite (a, b) and tetragonal martensite (c, d).^[44]

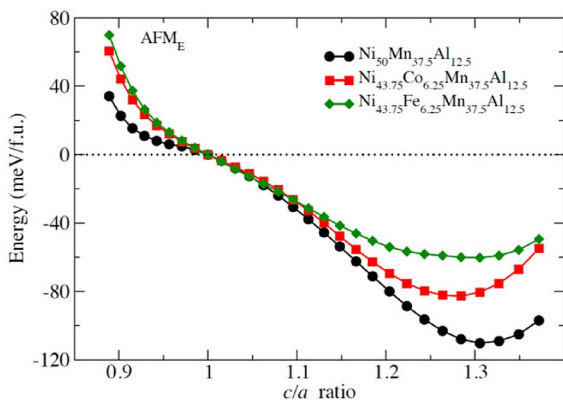


Figure 8. Total energies as function of tetragonality in the AFM_E states of $\text{Ni}_{50}\text{Mn}_{37.5}\text{Al}_{12.5}$, $\text{Ni}_{43.75}\text{Co}_{6.25}\text{Mn}_{37.5}\text{Al}_{12.5}$, and $\text{Ni}_{43.75}\text{Fe}_{6.25}\text{Mn}_{37.5}\text{Al}_{12.5}$.^[44]

isothermal entropy change between different crystallographic directions.^[46] For these investigations, Pt-doped $\text{Ni}_{2-x}\text{Pt}_x\text{MnGa}$, has been chosen as the substitution of Pt for Ni increases the martensitic transition temperature in these alloys (see Figure 2). As Pt is a 5d element with almost an order of magnitude larger spin-orbit coupling parameter than Ni, the general expectation is that the substitution of Pt will increase the MAE in $\text{Ni}_{2-x}\text{Pt}_x\text{MnGa}$. Contrary to our expectation, both experimental measurements and theoretical calculations^[47] have shown a slightly decreasing trend in the MAE with increasing Pt content (Figure 9). Interestingly the calculated orbital moment anisotropy (OMA) also shows a similar trend to the MAE, which suggests a direct relation

between the MAE and the OMA, similar to what has been investigated previously in many other systems.^[48] The origin of this unexpected trend in the MAE lies in the interplay of chemical and elastic changes due to Pt doping. Our theoretical calculations have revealed that the chemical and structural changes due to Pt doping influence the MAE in an opposite way. The increase in the MAE due to chemical effects (i.e., the larger orbital moment of Pt) is compensated by the dominant elastic effect (larger c/a ratio due to Pt), which determines the resulting composition-dependent changes in the MAE in these alloys.

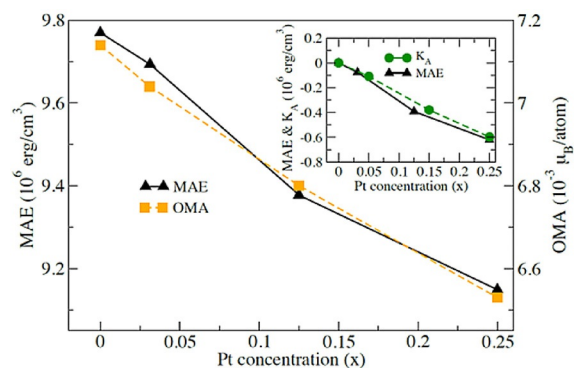


Figure 9. Dependence of the MAE and the OMA on the Pt concentration in $\text{Ni}_{2-x}\text{Pt}_x\text{MnGa}$ as obtained from ab initio calculations. The inset shows the variation of the theoretically calculated MAE and the experimentally determined K_A with increasing Pt concentration. Both quantities in the inset are plotted taking their respective values for Ni_2MnGa as a reference.^[47]

2.4. Coupling at interfaces in multilayers

Tuning material properties by combining different systems in a layered structure has become a well-known route in materials science.^[49] The direct contact between different materials, as it would happen in layered structures leads to coupling phenomena across the interface, which can give rise to functionalities beyond their individual bulk properties. This is also expected for magnetocaloric cooling devices, for which recent investigations highlight the importance of such couplings in multi-layered regenerators.^[50] One of the processing strategies is, for example, the extension of the operating temperature range by employing composites.^[51] Another scheme is the combination of the conventional^[52] and inverse^[5] MCE into a single system^[53] such that the iMCE material can be used as a heat-sink for the heat generated by a cMCE material when it is magnetized before cooling by adiabatic demagnetization^[5,54] The class of $\text{Ni}_2\text{Mn}_{1+x}\text{Z}_{1-x}$ Heusler materials offers an optimum model system for this as it contains materials showing both the iMCE (e.g., $\text{Z}=\text{Sn}$) and the cMCE (e.g., $\text{Z}=\text{Ga}$).

Recently, the coupling phenomena at Ni–Mn–Sn/Ni–Mn–Ga interfaces in epitaxial films have been studied. The focus was to understand the structural and the magnetic coupling between the two sub-systems (Ni–Mn–Ga and Ni–Mn–Sn) upon putting together in a layered structure. For the theoretical ab initio study, a 64 atom supercell has been considered, as shown in Figure 10.

On the one hand, in-plane and out-of-plane lattice constants have been considered for such bilayer systems.^[10] The ab initio studies could well reproduce the bulk lattice parameters for $\text{Ni}_{51}\text{Mn}_{35}\text{Sn}_{14}$ and Ni_2MnGa , but with the additional challenge that the experimentally determined strains of the Ni–Mn–Sn/ Ni_2MnGa system could not be explained solely by

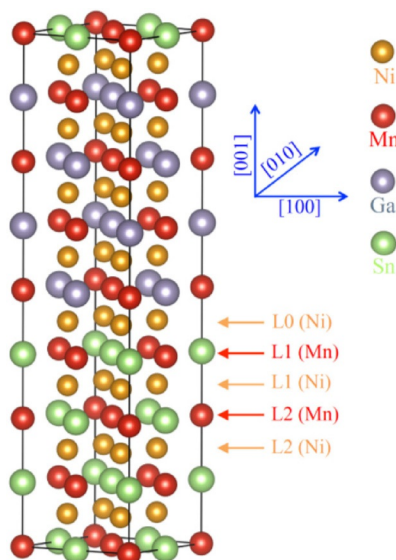


Figure 10. Schematic representation of the 64 atom supercell used to simulate the $\text{Ni}_2\text{MnSn}/\text{Ni}_2\text{MnGa}$ bilayer system. L0 indicates the interface where Ni atoms are present. L1 and L2 represent the second and third layers, respectively, of Ni and Mn atoms from the interface.

the lattice mismatch between the two Heusler materials and the expected Poisson effect. This was resolved by taking interdiffusion into account as an additional contribution that can occur due to the high deposition temperature (500°C), which is required for proper crystallization of the Heusler layers.

Our ab initio calculations have shown that the total energy of the system goes down (by 154 meV per cell) if a Ga atom switches position with an excess Mn atom in the Ni–Mn–Sn layer. As Ga atoms are slightly larger than Mn atoms, this leads to an increase of the out-of-plane lattice parameter, unit-cell volume, and c/a ratio of the Ni–Mn–Sn layer and subsequently a decrease in all three parameters for the Ni_2MnGa layer. Other exchanges of atoms, as between a Ga atom and a host Mn atom in Ni–Mn–Sn and between a Ga atom and a Sn atom, increase the total energy of the system and hence are unfavorable.

This prediction is in agreement with Auger electron spectroscopy experiments that have shown interdiffusion of Ga (and no other atomic species) throughout the whole thickness of the Ni–Mn–Sn film.^[10] Consequently, an interplay of strain and interdiffusion determines the structural properties of the bilayer system. Considering that the martensitic transformation temperatures sensitively depend on the chemical composition, the functional properties of both Heusler films will be significantly altered, which makes it very difficult to use Ni–Mn–Sn and Ni–Mn–Ga in a multilayer system for a mutual interplay of conventional and inverse MCE.

On the other hand, the calculations have revealed that both the magneto-elastic coupling and the chemistry influence the atomic spin moments in the bilayer system. The chemical effect (interface between Ga and Sn layers) turns out to dominate and to remain mostly localized in the proximity of the interface.^[9] The MAE, that is, the energy gain for a magnetization along the easy axis with respect to the hard axis, is however rather tiny ($\text{MAE} = E_{100} - E_{001} \approx 50 \mu\text{eV}$ per cell) for the bilayer system. An investigation of the atomic orbital moment (μ_l), which is closely related to the MAE in many materials, however indicates that there is significant anisotropy present in each layer (Figure 11). The Ni orbital moments at the interface change by approximately 40% compared to the Ni orbital moments in the inner layers. More importantly, the orbital moment anisotropies $\Delta\mu_l$ (difference of orbital moments between the easy and hard axes) for both Ni and Mn atoms have almost equal and opposite values in the Ni_2MnGa and the Ni_2MnSn layers. This is one reason for competing contributions of the two individual layers in the bilayer system. Furthermore, the MAE values of bulk Ni_2MnGa and Ni_2MnSn have been evaluated.^[9] The two systems exhibit similar variation in the MAE upon tetragonalization ($c/a \neq 1$) with a change in sign of the MAE occurring at $c/a = 1$. As Ni_2MnGa and Ni_2MnSn have different c/a ratios in the bilayer system ($c/a < 1$ and $c/a > 1$, respectively), they again have competing contributions leading to the observed low MAE of the bilayer system. This cancellation of MAEs rules out the possibility of anisotropic magnetocaloric response^[55] in this bilayer system.

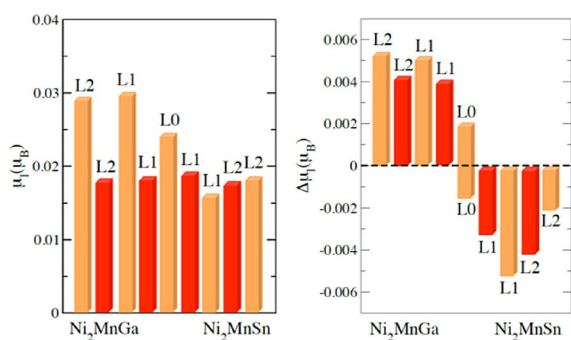


Figure 11. Local orbital moments μ_l for the magnetization along the [100] axis and anisotropy of the local orbital moments $\Delta\mu_l = \mu_{l,100} - \mu_{l,001}$ in different layers for Ni (orange) and Mn (red) atoms in the bilayer system. Figure taken from Ref. [9]. Copyright, World Scientific 2016. Reproduced with permission.

3. Stress Coupling

In addition to the atomic-scale coupling mechanisms, magnetocaloric materials, particularly those with a pronounced first-order transition, are often susceptible to external pressure.^[56,57] This is caused by the coupling between the magnetic transition (e.g., ferro- to paramagnetic) and a simultaneous change in volume and/or structure due to a stabilization of the low-volume phase.

The direction and strength of the effect depends on the type of the transition. Ni–Mn–In–Co Heusler alloys are MCE materials with a magnetostructural transition, in which an increase of the transition temperature by up to 40 K upon application of 0.84 GPa pressure is observed.^[58] Here, the low-temperature phase has the lower volume. Our ab initio calculations for Ni–Mn–Al–Co also show a similar trend. La(Fe,Si)₁₃ is an example for a magnetovolume transition, in which the cell volume decreases upon transition to the paramagnetic phase. Hence, the transition temperature is shifted to lower temperatures upon applying isostatic external pressure.^[59] The shift of T_C in LaFe_{11.18}Si_{1.82} can be as large as 35 K for a pressure of 0.5 GPa.^[60] For porous samples, for example, LaFe_{11.6}Si_{1.4} with a porosity of 20 vol %, an even larger change in the transition temperature of 96 K with $\Delta p = 0.9$ GPa^[61,62] is observed. For bulk materials, applying isostatic internal or external pressure can be thought of something happening on a global scale, leading to similar effects throughout the whole sample. For porous materials, local influences of pressure become visible,^[61] which are also present in bulk materials but are more easily overlooked.

A reverse (i.e., tensile) pressure can be achieved by alloying with dopant elements such as hydrogen, boron, carbon, or nitrogen. Adding these elements enlarges the crystallographic cell by as much as $\Delta V = 0.4\%$ for interstitial hydrogen and $\Delta V = 1.7\%$ for carbon in La(Fe,Si)₁₃.^[63] Particularly efficient for shifting the transition temperature while at the same time preserving the magnetocaloric effect is hydrogenation such as, for example, in La(Fe,Si)₁₃H_x,^[64] as it leaves the electronic structure nearly unchanged compared to the un-

doped state.^[63] In this case, the transition temperature T_C increases by approximately 135 K in LaFe_{11.44}Si_{1.56}H_{1.6} as compared to the unhydrogenated material,^[65] whereas the lattice parameter increases isotropically.^[66] Hence, external isostatic pressure and internal pressure due to, for example, hydrogenation are antagonistic drivers for shifting the transition temperature.

Uniaxial, tensile or compressive stresses, which usually stabilize low-symmetry phases in materials with structural transformations and are the external stimuli of elastocaloric effects,^[13] have also been used to control the transformation temperatures of magnetocaloric materials.^[67] For the sake of brevity we do not discuss them in detail, but emphasize instead the impact of biaxial stresses. They can occur due to the stress coupling of epitaxial thin films of magnetocaloric materials to a substrate (see Section 3.3). In materials with a magnetostructural transformation, the symmetry of the substrate surface can favor one of the involved phases over the other and lead to an incomplete transformation. This behavior can be optimized by the choice of the right substrate material.^[68] In materials with magnetovolume transformations, the biaxial strain caused by the lattice mismatch can be used to tune the transition temperature.^[69]

3.1. Volume effects

Materials such as La(Fe,Si)₁₃, which undergo a considerable volume change (up to 1.5 vol %^[70]) during the transition, will choose a minimum energy path to transform, which has a direct impact on the nucleation sites of the transition. For a cubic or rectangular sample, regions close to the corners, which are the least constrained, can expand more easily than those in the center of the cube.^[57] Therefore, during the transition to the ferromagnetic state, which is connected with an increase in cell volume, the transition is likely to proceed from the corners across the entire surface and then towards the center. This stress-coupling mechanism has been suggested as an interpretation of experimental in situ X-ray diffraction (XRD) data^[71] and from in situ magneto-optical imaging.^[72] Recently, finite-element simulations using a mechanically coupled ensemble of 1000 cubes confirmed this type of transition behavior.^[57] The observed existence of a long-range elastic interaction between different parts of a sample led to the speculation that also in magnetocaloric Heusler compounds, the elastic stress originating from the volume change at the MT can influence nucleation patterns, and is even proposed to lead to “auto-nucleation” of further nuclei in the strain field of a preceding nucleus.^[73] One of the consequences of selective nucleation at the corners of a cuboid sample is that the central part of the sample is put under pressure, which leads to a shift of the transition temperature for these regions and delays the further progress of the transition. As this only happens for the transition with expanding cell volume [e.g., the cooling transition in La(Fe,Si)₁₃], and the reverse transition is unaffected, an asymmetry in the progress of the heating and cooling transition is observed.^[71] Consequently, the development of strain in the sample is also

asymmetric with cooling and heating,^[74] and is much more pronounced for the expanding cell.

The exertion of pressure or strain on a sample is not limited to an active external or internal force as with the strain fields that occur during the magnetovolume transition. Strain can also be stored passively in a material after mechanical deformation (e.g., through milling). It has been observed that the magnetocaloric effect depends to some degree on mechanical pulverization and hence particle size,^[75] and that the transformation can even be completely suppressed below a certain threshold size (e.g., in Mn–Fe–Ni–Ge^[76]) or enhanced by decreasing the particle size (for LaFe_{11.8}Si_{1.2}^[77]). For magnetocaloric materials with magnetovolume (i.e., isostructural) transitions (e.g., LaFe_{11.8}Si_{1.2} and Mn_{1.2}Fe_{0.68}P_{0.5}Si_{0.66}), a sharpening of the transformation, but at the same time a broadening of the thermal hysteresis, is observed upon reducing the particle size.^[57] Hence, the suppression of the transformation due to strain is preceded by an increase of hysteresis, progressively preventing the particle from transforming.

The contrary situation, that is, the sudden release of mechanical strain together with a sharp decrease of thermal hysteresis, is observed during the so-called virgin effect in magnetocaloric materials.^[4] It is usually associated with the formation of cracks and hence a mechanical decoupling of different sample regions.^[71] It has been postulated recently that this mechanical decoupling itself causes the large difference in, for example, the entropy change or adiabatic temperature change between the first and further cycles, and is hence a stress-release caloric effect that occurs only in the first cycle.^[57]

3.2. Surface defects

The influence of local strain fields on the transition can also be observed at the surface of bulk materials, or in thin films with large surface-to-volume ratios. Again, the strain fields at the surface can lead to preferential nucleation sites and to a shift in local transition temperatures. Strain fields at the surface of a sample can be caused by morphological features and defects. For instance, the shift of the transition temperature in the vicinity of an artificial mechanical defect (induced by plastic deformation with a nano-indenter tip) in a thin film of Ni_{48.4}Mn_{32.8}Ga_{18.8} was studied by Niemann et al.^[78] In these magnetocaloric Heusler compounds, the martensitic transition can be induced by stress, either globally,^[79,80] or locally.^[78] The latter stress-induced martensite formation can be tracked by atomic force microscopy (AFM) imaging, revealing an elastic stray field around the defect that locally influences the martensite start temperature and globally has an impact on the hysteresis of the transformation. Unlike mechanical defects, the surface morphology of a non-flat sample does not exert strain on the transforming material per se. However, surface features such as scratches, which have a cross-sectional morphology similar to indents,^[81] can enhance or attenuate the impact of the volume change that is associated with the transition. For convex regions at the sample

surface, a scenario similar to the one described for the corners of a cube applies (see Section 3.1): nucleation is facilitated at convex regions if the volume increases during the transition. On the other hand, for concave regions nucleation is suppressed due to the strain fields that build up more easily in such confined geometries.^[82] Local strain fields produced by strongly concave and convex surface morphologies can therefore lead to local T_C shifts comparable with the effect of hydrostatic pressure. On the other hand, the absence of strain fields in flat regions of the sample leads to a uniform growth of the ferromagnetic phase. Though it has only been shown partly in experiments to this point, it is feasible to assume that nucleation and growth and hence also the thermal hysteresis can be tuned by the surface shape of a sample, opening up a promising way to control the extrinsic properties of magnetocaloric materials. One should note, however, that these are results of temperature-driven transitions, but transitions in magnetocaloric materials can be driven by both changing external magnetic fields and temperature.^[83] For the case of a magnetic-field-induced transition, competing influences of strain and the demagnetizing field are expected.^[84]

3.3. Epitaxial thin films

In epitaxial thin films the stress coupling to the substrate plays an important role for the magnetocaloric properties. This kind of coupling is especially important for first-order materials as those rely on structural transformations. It was observed in several investigations^[85,86] that a full MT does not occur in thin films that are bound to rigid substrates. To achieve a deeper understanding of that phenomenon, in a recent study, the Heusler material Ni–Co–Mn–Al was grown epitaxially on different substrates/buffer layers to determine the dependence of the underlayer on the MT by temperature-dependent XRD experiments.^[68]

The integrated intensity of the fundamental (004)_A peak of the austenite was taken as a measure for the fraction of austenite in the sample (see Figure 12a). Three different underlayer materials that favor epitaxial growth of the Heusler material in the [001]_A direction were investigated: MgO(001) and MgAl₂O₄(001) substrates and vanadium (V) seed layers [MgO(001)(substrate)/V(001)(30 nm)]. It was observed that the martensitic transition was incomplete in all investigated cases, but the amount of residual austenite varied significantly depending on the underlayer material from 15% for V to 40% for MgAl₂O₄. The oxide underlayers MgO and MgAl₂O₄ hindered the MT more severely than a 30 nm vanadium underlayer.

It seems obvious that the coupling to the substrate hinders the transformation of the adjacent material. Figure 12c shows the amount of residual austenite versus the lattice mismatch of the underlayer to the Heusler layer. The most complete transformation is reached for the largest lattice mismatch of 4%, which is somewhat contrary to the naive assumption that a minimum lattice mismatch is favorable for a complete transformation. Similar to the surface defects dis-

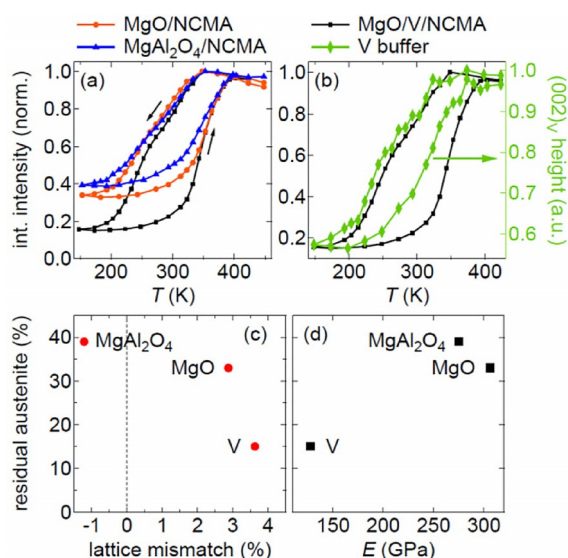


Figure 12. Martensitic transformation of Ni-Co-Mn-Al (NCMA) for different buffer layers. (a) The temperature dependence of the normalized integrated intensity of the (004)_A peak is taken as a measure for the phase fraction of austenite. The amount of residual austenite depends on the underlayer, but the temperature interval of the transformation does not. (b) Impact of the MT on the V buffer. The height of the (002)_V peak changes significantly during the MT of the Ni-Co-Mn-Al film on top and exhibits hysteresis. The black curves in all figure parts (right axis) show the MT. (c, d) Residual austenite in dependence of the lattice misfit (c) and Young's modulus (d). For a complete MT, small positive lattice misfit and an elastic underlayer are beneficial.^[68]

discussed in Section 3.2, it is possible that misfit dislocations, which reduce the strain in the film close to the underlayer, can act as nucleation centers for the martensite. It is also striking that the amount of residual austenite differs only slightly between MgAl₂O₄ and MgO, where the difference in lattice constant is 4.1 %, and strongly drops from MgO to V, where it is only 0.7 %. This indicates that the lattice mismatch is not the only influence on the transformation.

First-principles investigations provide further insight into the underlying mechanism. They confirm that a fully coherent coupling to a rigid substrate would suppress the MT completely. The V underlayer of the samples is evaluated for Figure 12, however, it has a limited thickness and a small Young's modulus, which allows the seed layer to partially adapt to the transforming Heusler film. Based on this assumption, a self-consistent scheme has been considered, where the Heusler film and the seed layer are elastically coupled and mutually influence each other. As they share in the coherent regime with the same in-plane lattice constant, any tetragonal distortion of the Heusler film will result in a corresponding Poisson expansion in the V underlayer perpendicular to the interface. Both parameters, the in-plane lattice constant and the Poisson expansion, are determined at each step of the MT such that the elastic energy of the combined system is minimized.

According to this scheme, first-principles calculations have been performed for different *c/a* ratios along the Bain path

for Ni-Mn-Al Heusler films. In agreement with the experimental observation, the adaption of the underlayer turns out to allow for a more complete MT, in contrast to the situation for rigid substrates. The resulting Poisson distortions of the V seed layer are small in the austenite but should be clearly noticeable in the martensite phase. However, detailed values depend on the relative thickness of the Heusler film and the V underlayer. This highlights the mutual coupling of both materials. The calculations further indicate that the martensitic transition temperature in the Heusler/V system will be lower than that of the corresponding bulk Heusler material. On the one hand, this can be concluded from the energy profile of the Bain distortion at $T=0$ K. On the other hand, the structural coupling has been proven to have a significant effect on the lattice vibrations in the Heusler film. The consequences of these observations are still subject to investigations.

From experiments, in qualitative agreement with the first principles calculations, the underlayer with the lowest Young's modulus (vanadium) allows the most complete MT of the adjacent Heusler layer (see Figure 12d). Also, indications that the V underlayer is distorted during the MT of the Heusler layer, were observed (see Figure 12b). The height of the V(002) peak decreases by 40 % during the MT and recovers upon heating, however, at lower temperatures than the reverse transformation of the Heusler layer. The interpretation is that upon heating, when the martensite becomes unstable, the restoring force of the elastically deformed V causes some reverse transformation of the Ni-Co-Mn-Al close to the V layer, whereas the bulk of the Heusler film requires further overheating for a complete transformation.

Although uniaxial strain (compressive or tensile) usually favors the martensite state, as it can minimize the strain energy by rearranging the martensitic variants,^[13] this biaxial, epitaxial strain favors the austenite. It is noted that the lattice mismatch between the cubic substrate and the epitaxially grown austenite has no significant impact on the average transformation temperatures of the rest of the films (see Figure 12a and Ref. [68]). A shift of the transition temperatures that is dependent on slight differences in the lattice mismatch is, however, observed in other material families that exhibit magnetovolume transformations. For example, in epitaxial FeRh films, a tensile epitaxial stress was observed to stabilize the high-volume phase, whereas a compressive stress destabilized it.^[69] By variation of the substrate and capping layer, the in-plane lattice parameter was strained by up to 0.6 %, allowing a tuning of the FM-AFM transformation temperature over a ≈ 50 K range (373–425 K). The film thickness in that experiment was 30–50 nm, which is less than the expected critical thickness for the formation of dislocations. This is not observed in our investigation of Ni-Co-Mn-Al films, on the one hand because of the high film thickness of 200 nm and the formation of misfit dislocations close to the substrate, which lead to relaxation of the lattice constant. On the other hand, the martensite phase has different symmetry from the austenite and therefore a cubic substrate lattice that fits well to the austenite does usually not fit to the mar-

tensite. A cubic substrate then favors the cubic austenite regardless of a small lattice misfit.

Additional information on the substrate impact was gained by studies on the film thickness dependence of the MT in epitaxial films. For this, magnetocaloric Ni–Mn–Sn films with thicknesses between 10 and 200 nm on MgO substrates were investigated (see Figure 13). It was observed by resistivity measurements that a thickness-independent amount of the Heusler material remains in the austenite state. Also, with increasing film thickness the transformation range significantly narrows, and the transformation temperatures increase and converge at high film thickness.

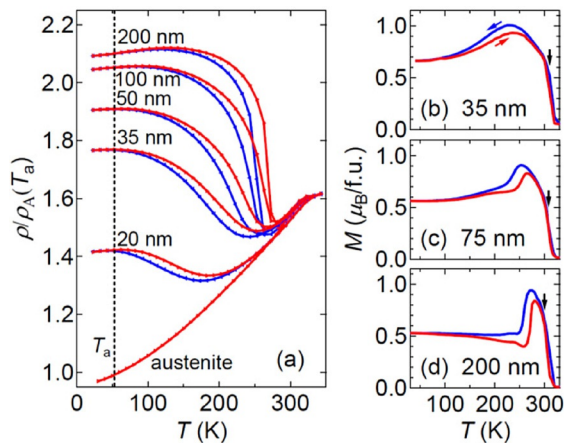


Figure 13. Film-thickness dependence of the MT. The changes in resistivity (a) and magnetization (b–d) are more pronounced for thicker films. This indicates an amount of residual austenite close to the substrate. $M(T)$ was measured at low external field: $\mu_0 H_{ext} = 5$ mT. The vertical black arrows indicate the Curie temperatures. The blue and red arrows indicate field cooling and field heating, respectively.^[87]

Another point that should be considered regarding the MT in epitaxial films on a substrate is the crystallographic coupling at the austenite/martensite interface and the substrate/martensite interface in particular.

The nucleation and growth of martensite in epitaxial films was investigated in detail by Niemann et al.^[88] The MgO(001) surface does not form a coherent interface with the martensite, and thus the martensite can only meet the substrate along a line. Therefore, a transformation of austenite in the vicinity to the substrate requires the formation of many small martensitic nuclei. This is energetically unfavorable due to the high surface-to-volume ratio of the nuclei and hence requires undercooling and leads to an incomplete transformation.

For adaptive 14M martensite, which is found for example, in Ni–Mn–Ga and Ni–Co–Mn–Al,^[7,43] the martensitic nuclei are elongated and flat diamonds with habit planes inclined by few degrees from the $[011]_A$ direction and an aspect ratio of approximately 40:14:1.^[88] The maximum size is determined by one tip of the diamond touching the substrate (see Figure 14) because a larger nucleus requires a finite interface with the substrate, which is energetically vastly unfavorable.

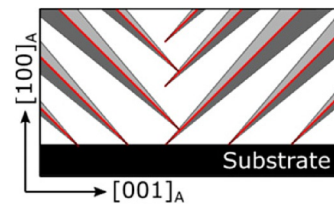


Figure 14. Model of martensitic nuclei in a film cross-section.^[88]

Thus, the film thickness dictates the maximum size of a martensitic nucleus. The consequence is that with decreasing film thickness the nucleation requires more undercooling which shifts the transformation to lower temperatures.^[87,89] The nuclei grow mainly in length and not in width because they cannot form a finite interface with the substrate.

As a last point on this topic, we want to examine what happens when an epitaxial film is detached from the substrate. A common way to do this is to prepare the films on a sacrificial seed layer that can be selectively etched. This has been shown for magnetocaloric Heusler thin films, for example, with Cr or the above-mentioned V seed layers.

Figure 15 shows the transformation temperatures of freestanding and substrate-constrained Ni–Co–Mn–Al films with dependence on the valence electron concentration. Clearly, T_M and T_A decrease with decreasing e/a ratio, as expected for Ni–Mn-based Heusler compounds.^[13] Furthermore, it is visible that the MT occurs at higher temperature when the film is released from the substrate and the substrate constrained films with low e/a ratios show no or only incomplete MT. Clearly, the epitaxial strain that, as mentioned above, stabilizes the austenite is now omitted, which can explain this effect. However, other influences are also likely to play a role. Without a substrate, the maximum size increases and the surface-to-volume ratio of the martensitic nucleus decreases. That means that the increase in surface energy due to the new martensite/austenite interface is compensated by

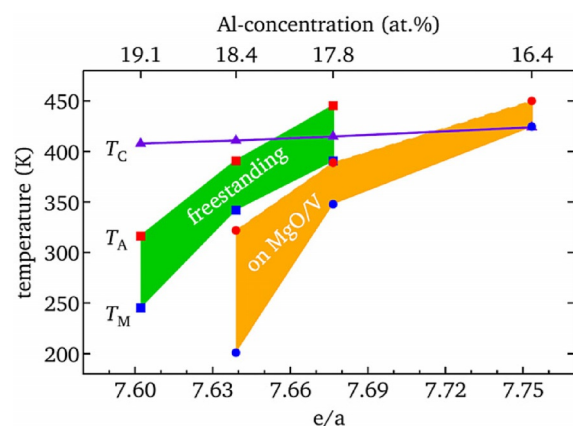


Figure 15. Structural phase diagram of freestanding and substrate-constrained Ni–Co–Mn–Al films. The transformation temperatures are shown as a function of the e/a ratio. T_M and T_A are shown by blue and red symbols, respectively. The orange and green areas represent the transformation range of the substrate constrained and freestanding films, respectively.^[90]

the decrease in volume energy at higher temperature. Furthermore, it was observed^[90] that the martensitic microstructure in freestanding films is different to that of constrained films and therefore the Gibbs energy of the martensite phase may vary, which would lead to different transformation temperatures. However, a detailed study on the microstructure and the nucleation process in free-standing thin films as well as an extensive comparison of different magnetocaloric Heusler materials is not yet present.

4. Magnetostatic Coupling

It is known that external static magnetic fields can shift the transition temperature in magnetocaloric materials by as much as $\mu_0^{-1}dT_C/dH=4\text{--}5\text{ K T}^{-1}$ for Curie ferromagnets,^[91] as they stabilize the magnetically ordered phase during the transition. Internal magnetostatic fields are primarily considered only in terms of the internal demagnetizing field, which counteracts the external field depending on the global sample geometry.^[92] The demagnetization field along the long axis of needle-like shaped bodies and the in-plane direction of thin films can be neglected.^[93] Nevertheless the demagnetizing field must be accounted for in all other sample geometries, as the entropy change of magnetocaloric materials will be underestimated if the demagnetization field is neglected.^[94] This can be challenging when the sample shape is far from simple geometric bodies such as ellipsoids or spheres. For a packed bed of spheres, which is a common geometry for magnetocaloric heat exchangers, numerical finite-element simulations showed that local demagnetizing fields vary by approximately 6.0–6.7%.^[95] It is furthermore shown that the demagnetization factor is only slightly dependent on the density and size distribution of the packed spheres (monodisperse, normal-, and log-normal distributions), for the considered porosity values between 40 and 60%. As with the global magnetic dipole interaction, which can have a significant impact on the kinetics of nucleation and growth during the transition,^[84] local demagnetizing fields can have strong implications for the distribution of local transition temperatures through the heterogeneity of the magnetic field they induce. For instance, Refs. [96,97] showed that the local distribution of demagnetizing fields can lead to broadening of the transition.

Furthermore, the local magnetic fields produced by the sample itself either by ferromagnetic minority phases (e.g., α -Fe in La(Fe,Si)₁₃, see Bennati et al.^[72]) or grains that have already turned ferromagnetic present magnetostatic stray fields for neighboring sample regions. This consideration will also be relevant for multilayers of magnetocaloric materials (see Section 2.4). For the case of α -Fe precipitates, it is difficult to distinguish transition temperature shifts close to the precipitates originating from chemical inhomogeneity from those due to magnetic stray field interaction. For particles or sample fragments, magnetostatic interaction between those is easier to study. Though mostly relevant for temperature-driven transitions with no external magnetic overriding the impact of the weak stray fields, interesting observations of

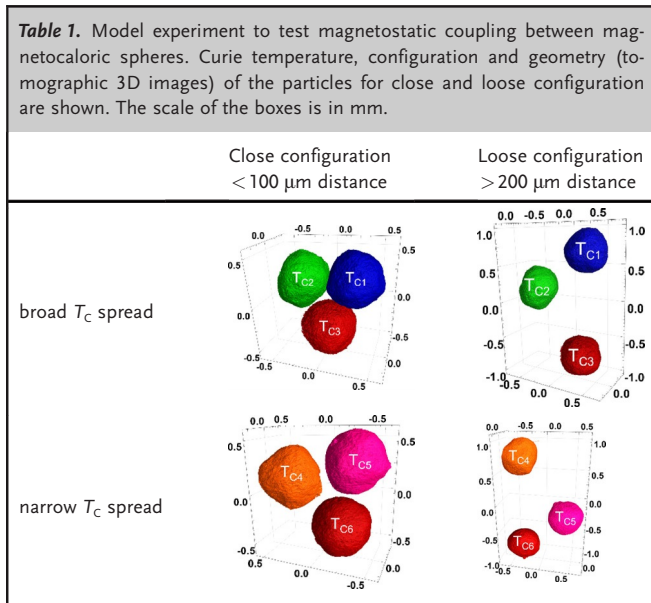
magnetostatic coupling phenomena between particles and across air gaps of bulk material have been made and will be described in the following.

4.1. Across cracks and gaps

There is experimental evidence^[71,96] that magnetostatic coupling in an ensemble of fragments/particles in close contact leads to sharpening of the transition compared to when the particles are further apart. The transition to the ferromagnetic state is facilitated by dipolar coupling leading to nucleation in neighboring particles.^[98] For dipolar coupling, no direct particle contact is required, and this mechanism works even across cracks and between weakly connected regions.^[96] The most important implication of this observation is that cracks, which are one of the mayor challenges in the application of magnetocaloric materials, do not necessarily compromise the sharpness of the transition. The work of Cohen et al.^[99] implies that as long as samples retain their envelope shape, cracks will not be deleterious. Waske et al.^[71] came to the conclusion that crack formation is helpful to reduce thermal hysteresis and is not in contradiction to maintaining a sharp transition. Similarly, Lovell et al. showed that magnetic field hysteresis reduces in fragmented and separated samples, which has been shown to be caused by a shift in the onset field of the transition.^[96] In this case, it is again local changes in demagnetizing fields introduced by edges and asperities that influences the onset of the transition.^[99] Magnetic dipole coupling is a weak interaction, and there are many cases where it does not play a significant role (e.g., Ref. [100,101]). If only temperature-driven transitions without external field are considered, there must be a set of minimum requirements for magnetostatic coupling between particles to occur. As in the literature both coupling and non-coupling are observed, and a model experiment is used in the following section to clarify under which conditions magnetostatic coupling can be expected to occur.

4.2. Between model spheres

In the following model experiment, we use spherical magnetocaloric particles and vary i) the distance between them and ii) the difference in their transition temperatures to study if magnetostatic coupling is observed. We use nearly spherical magnetocaloric particles of La(Fe,Mn,Si)₁₃H (“CALORIVACH”) supplied by Vacuumschmelze, Germany with nominal diameter of $d=600\text{ }\mu\text{m}\pm 3\text{ }\mu\text{m}$. The magnetization as a function of temperature of each sphere has been determined by using a superconducting quantum interference device (SQUID) magnetometer, and the transition temperature of each sphere was determined from the minimum of the first derivative of the $M(T)$ curve. Sets of three particles each have been selected by their transition temperature. The first one (“broad TC”) has transition temperatures of $T_{C1}=287.8\text{ K}$, $T_{C2}=291.3\text{ K}$, and $T_{C3}=294.8\text{ K}$. The second one (“narrow TC”) has transition temperatures of $T_{C4}=292.1\text{ K}$,



$T_{C5}=293.3$ K, and $T_{C6}=294.1$ K. In Table 1 the geometric configurations are shown.

The particles with “narrow” and “broad” transition temperatures have been assembled into two different ensemble configurations with varying physical distance: i) the “close” configuration with a mean distance of 30–50 μm for broad T_C spread and 50–80 μm for narrow T_C spread, ii) the “loose” configuration with mean distance of 250–500 μm for broad T_C spread and 400–1000 μm for the narrow T_C spread. The particles have been mounted on Kapton tape. The distances have been determined from 3D images of the ensemble imaged with an X-ray computed tomograph (XCT).

With a SQUID magnetometer, isothermal magnetization measurements at fields up to $\mu_0 H=2$ T have been performed to determine the magnetization curves and the entropy change for the individual particles, as well as for the ensembles. From isothermal magnetization measurements ($\Delta\mu_0 H=0$ –2 T, $\mu_0 H=0.1$ T steps) the entropy change was calculated using the Maxwell relations.^[102] For comparison, the average curves for the magnetization measurements and the entropy change of the ensembles were calculated by a weighted average of the individual curves. Furthermore, the switching behavior of the “narrow” transition temperature sphere ensemble was studied using magneto-optical imaging. A Peltier element was used to heat and cool the particle ensemble, on which the particles were mounted. A magneto-optical indicator film on top of the particles, indicated the magnetic stray field out of the imaging plane. The background was subtracted from the images to visualize only the magnetic transition. The temperature was measured using a thermocouple. A magnetic field of strength $\mu_0 H=0.1$ T was applied in the out-of-plane direction. More details concerning the experimental setup are presented in Funk et al.^[100]

In Figure 16, the magnetization (top) and entropy changes (bottom) of the individual particles with “broad” transition

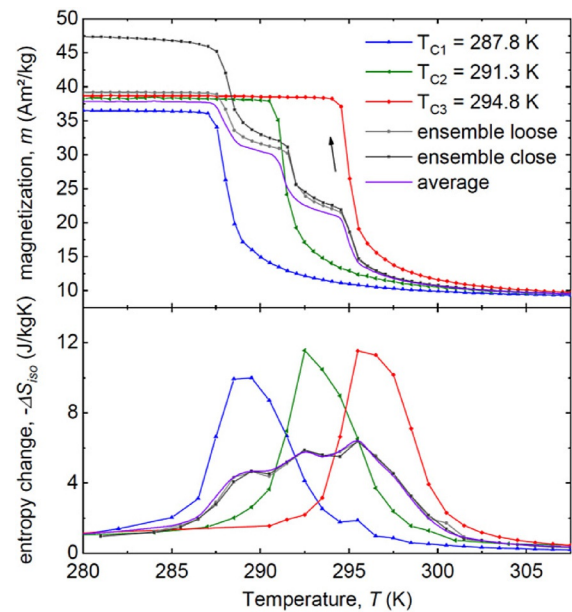


Figure 16. Magnetization ($\mu_0 H=0.1$ T) and entropy change ($\Delta H=1$ T) of the experiment with the broad transition width as a function of temperature.

temperatures and corresponding ensemble configurations (“close” and “loose”) are shown. The measurement of the ensemble is nearly identical to the weighted average of the individual particles for both quantities. Hence, there is no evidence for coupling between the particles, which thus transform independently of each other. The only thing one notes is the larger magnetization of the “close” configuration than those of the “loose” one or the weighted average of the individual particles. This is probably due to a decreased influence of the demagnetizing field when particles are closer together (see Ref. [95]), and hence to larger total values of the magnetization. In Figure 17, the magnetization upon cooling (top) and the entropy changes (bottom) of the individual particles with “narrow” transition temperatures and their two ensemble configurations (“close” and “loose”) are shown. In the magnetization curves, an ensemble behavior strongly deviating from the average weighted sum of the individual particles is visible. Upon cooling, we observe that all three particles transform together at a transition temperature that is identical to the highest transition temperature of the three particles involved ($T=294.1$ K). The shape of the resulting $M(T)$ curve is created by three particles acting together, nearly simultaneously. Only two very slight shoulders indicate that it is actually composed of three contributions. We conclude that the magnetic stray field created by the particles with the highest transition temperature ($T_C=294.1$ K) leads to magnetostatic coupling between the particles, thereby inducing nucleation and growth of the ferromagnetic phase in the two neighboring particles as well.

For the narrow distribution of the Curie temperatures, the entropy change was calculated for the individual particles, as well as for the ensembles (see. Figure 17, bottom). The ensembles have an entropy change value comparable to the individual particles. It is slightly higher than the expected

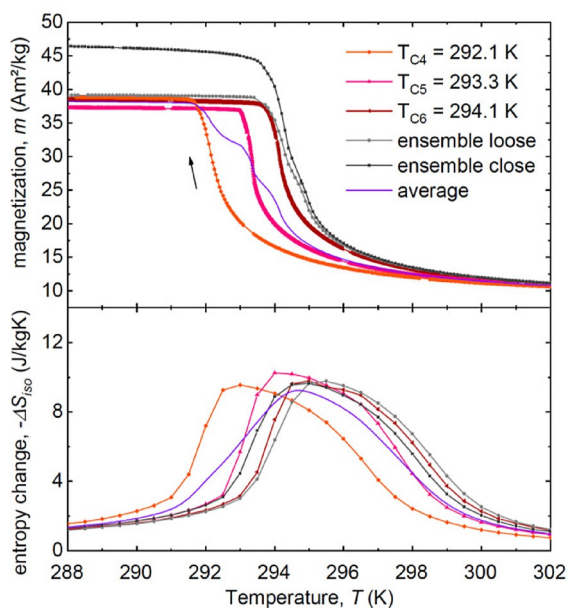


Figure 17. Magnetization ($\mu_0 H = 0.1$ T) and entropy change ($\Delta H = 1$ T) of the experiment with the narrow transition temperature distribution as a function of temperature.

value from the weighted average and the transition is shifted to higher values. Thus, the magnetocaloric properties of the ensemble do not behave as individual particles, but as one bulk. To provide further evidence for the coupling we observed in the magnetization curves of the ensemble with narrow transition temperatures, the particle ensemble was studied using magneto-optical imaging (see Figure 18). For magneto-optical measurements the particles were fixed with silver paste in the “loose” configuration (distance = $500 \mu\text{m}$) and additionally a “far” configuration with $1800 \mu\text{m}$ distance (see insets in Figure 18) has been realized. The gray value corresponds to the magnetic moment, with dark gray indicating a larger magnetic moment than light gray. For two differ-

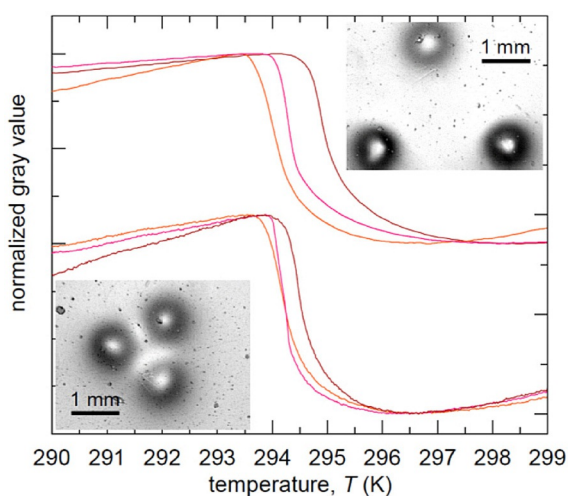


Figure 18. Normalized gray value for the $500 \mu\text{m}$ (bottom) and the $1800 \mu\text{m}$ spaced (top) particles during heating. The insets show the magneto-optical images at low temperatures.

ent configurations (“close” and “far”) it is observed that the particles switch individually when they are distant from each other ($d = 1800 \mu\text{m}$) and the transitions move closer together for the close configuration ($d = 500 \mu\text{m}$). Hence, this imaging experiment also provides evidence that magnetostatic coupling can occur for temperature-driven transitions under low field, for particles with narrow T_C distribution and in close proximity.

In Figure 19, an overview of magnetostatic coupling phenomena from this work and the literature is presented. On the x -axis, the distance between the particles, and on the y -axis the mean difference of their transition temperatures are plotted. In general, particle ensembles with a distribution of

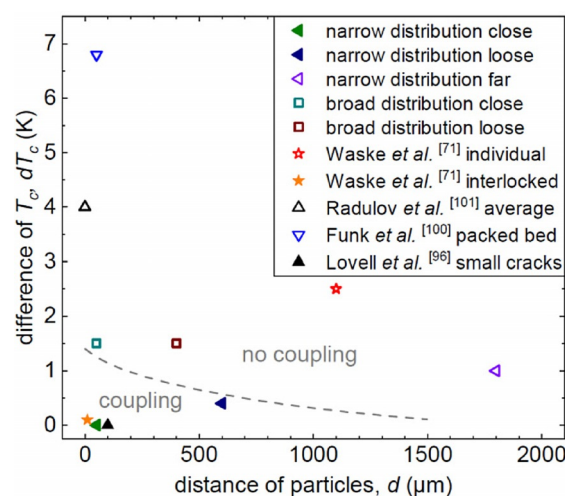


Figure 19. Magnetostatic coupling of magnetocaloric particles depending on their distance and their difference in transition temperature from literature and in this work. The data are from this work and from Refs. [71, 96, 100, 101].

transition temperatures that is too broad do not show magnetostatic coupling, even when the particles are very close. For particles in very close proximity ($d < 1000 \mu\text{m}$), the minimum requirement for coupling seems to be that the difference between their transition temperatures is typically less than $\Delta T_C < 1$ K. With this interpretation, it becomes clear why for example, Funk et al. [100] did not observe coupling in packed beds of very similar magnetocaloric particles. The distribution of transition temperatures, which in their case followed a Gaussian distribution with ($1.5 \text{ K} < \sigma < 2 \text{ K}$), was simply too broad. We expect that coupling within a packed bed of spheres can only occur for distributions of the transition temperature with $\sigma < 1$ K, which is typically not the case for the currently used packed beds of magnetocaloric materials. The large number of nearest neighbors (coordination number) of the packed bed probably might be able to reduce this upper limit in the variation of the transition temperatures further, but this is beyond the scope of this article and requires further investigations. To conclude, magnetostatic coupling between magnetic particles of an ensemble is a weak effect that requires precise control of the particles’ transition tempera-

tures and distances. In the best case, coupling can lead to entropy changes that resemble the bulk properties instead of a superposition of individual spheres, and it is therefore worth investigating further how magnetostatic coupling can be promoted in ensembles of particles and fragments.

5. Summary and Outlook

Strong coupling effects in magnetocaloric materials are the key factor to achieve large magnetic entropy changes in this material class. Combining experimental techniques on different scales with *ab initio* calculations, we have explored and exploited the relevant coupling phenomena, including atomic coupling, stress coupling, and magnetostatic coupling. For our investigations on atomic coupling, we have used the Heusler compounds as a point of departure. For thin films of many members of this material family, the chemistry, crystal structure, and microstructure can be readily controlled, and the step from perfect crystals to materials with imperfections, that is, composition changes and disorder, has been performed. Chemical interactions in multilayer films can lead to unusual strains and interdiffusion of distinct atomic species. Stress coupling occurs in first-order magnetocaloric materials, which exhibit a magnetovolume or magnetostructural transitions together with the magnetic transition. External stress can impact the phase transition of magnetocaloric materials and lead to, for example, a shift of their transition temperature or preferred nucleation sites. Though mechanical stress is typically exerted globally on the sample from the outside, it can also occur within the sample through the interaction of the volume expansion at the transition with sample features such as surface curvature or geometry. This can again lead to transition temperature shifts similar to those achieved by external pressure.

We have observed strong stress coupling in the volume and the surface of bulk materials, as well as between thin films and their buffer or substrate. The simulations reveal, in addition, that chemical and stress coupling have an impact on the lattice and magnetic degrees of freedom. Their coupling in turn is responsible for the response at the martensitic transformation temperature. Magnetostatic coupling has been experimentally demonstrated in magnetocaloric particles and fragment ensembles. It can significantly affect the progress of the magnetic transition and can finally lead to its sharpening if the fragments are in sufficiently close contact, thereby opening up a route to tune the width of the transition.

Epitaxial stress in thin films can lead to an incomplete MT in Heusler compounds that is dependent on the Young's modulus of the underlayer and has great impact on the martensitic microstructure. In materials with magnetovolume transformations, epitaxial stress can be used to tune the transformation temperature.

Magnetostatic coupling can occur between particles or parts of magnetocaloric material through the magnetic stray field of a ferromagnetic region or particle. In general external magnetic fields are able to shift the transition tempera-

ture in magnetocaloric materials, and it is therefore not surprising to find a similar, though more subtle effect for magnetostatic stray fields as well. Using a model experiment, we clarified that magnetostatic coupling between—and hence a cooperative behavior of—particles with different transition temperatures is observed as long as the transition temperatures are similar enough ($\Delta T_C < 1$ K) and the particles are in sufficiently close contact. Stress- and magnetostatic coupling are therefore important mechanisms influencing the functional properties of first-order magnetocaloric materials. It is important to note that the three levels of coupling effects discussed here occur in all samples simultaneously and mutually influence each other. We demonstrate this in Figure 20, which is a typical plot used for evaluating the atomic cou-

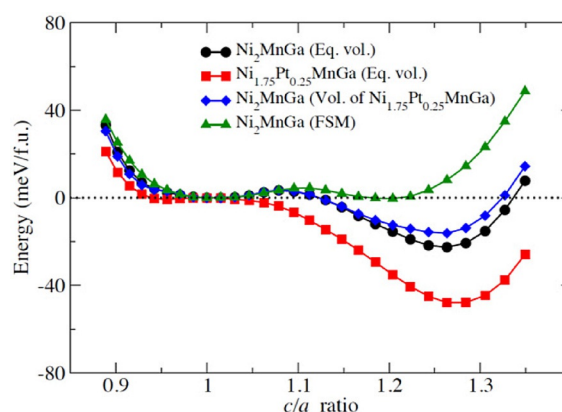
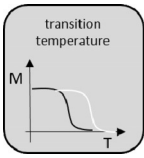
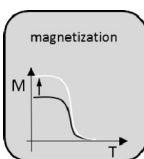
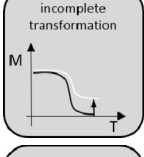
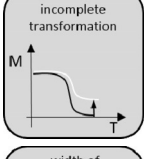
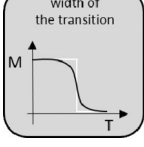


Figure 20. Total energies as function of tetragonality in Ni_2MnGa , including atomic, stress, and magnetostatic interactions.

pling in Section 2 (see Figure 8). The addition of Pt to Ni_2MnGa changes the relative stabilities of austenite and martensite (black vs. red line in Figure 20), which are decisive for the size of the MCE. At the same time, the addition of Pt changes the lattice constant. This kind of stress coupling alone, without the chemical effect of Pt, already has a noticeable impact on the austenite–martensite stability (black vs. blue line in Figure 20). We have furthermore pointed out the importance of magnon–phonon coupling for the MCE in Heusler alloys. A substantial part of it is already given by magnetostatic coupling effects. This is indicated in Figure 20 by comparing the austenite–martensite stability with and without reducing the magnetization to 5/6 of its saturated value within the fixed spin-moment (FSM) approach (black vs. green line in Figure 20). The effect is substantial and magnetostatic coupling effects will therefore influence the MCE in all real microstructures.

Based on the achieved insights, we have demonstrated that the functional properties can be tailored by tuning the occurring coupling phenomena to achieve the best magnetocaloric performance for cooling applications. Table 2 presents a summary of typical characteristics found in magnetocaloric materials; possible origins related to coupling phenomena are listed. With this overview, we hope to enable other researchers to more easily determine the reasons for typical behavior

Table 2. Impact of different coupling phenomena on characteristics of magnetocaloric materials.

| characteristics | possible origin [literature reference] |
|---|---|
|  | magnon-phonon coupling ^[26,28–31] thermo-chemical coupling ^[14,37,38,47] chemo-magnetic coupling ^[41,44,47] multilayer interface coupling ^[10] stress coupling in the volume, [57, 71] stress coupling in thin films, [85, 87] stress coupling at surface defects, [78, 82] magnetostatic coupling across cracks and gaps, [71, 96] magnetostatic coupling between particles, [this work] |
|  | magnon-phonon coupling, [32, 36] chemo-magnetic coupling, [42, 44] multilayer interface coupling, [9] stress coupling in the volume, [57] |
|  | stress coupling at surface defects, [78] stress coupling in thin films, [68] |
|  | stress coupling in the volume, [57, 72, 73, 79, 80] stress coupling at surface defects, [79, 80, 82] magnetostatic coupling across cracks and gaps, [96, 97] |
|  | stress coupling in the volume, [57, 71, 72] stress coupling in thin films, [85, 87] magnetostatic coupling across cracks and gaps, [71, 96, 99] magnetostatic coupling between particles, [this work] |

occurring in first-order magnetocaloric materials and other material classes with strong coupling effects at different scales.

Acknowledgements

All authors acknowledge support by the DFG priority program “ferroic cooling” (SPP 1599) under grants number WA3294/3-2, HU857/8-2 and HI1300/10-2. B.W. and A.W. thank VACUUMSCHMELZE GmbH & Co. KG for the supply of LaFeCoSi materials.

Conflict of interest

The authors declare no conflict of interest.

Keywords: ab initio calculations • ferroic cooling • Heusler alloys • magnetocaloric materials • magneto-structural transition

- [1] V. K. Pecharsky, J. K. A. Gschneidner, *Phys. Rev. Lett.* **1997**, *78*, 4494.
- [2] S. Y. Dan'kov, A. M. Tishin, V. K. Pecharsky, K. A. Gschneidner, Jr., *Phys. Rev. B* **1998**, *57*, 3478.
- [3] F.-X. Hu, B.-G. Shen, J.-R. Sun, Z.-H. Cheng, G.-H. Rao, X.-X. Zhang, *Appl. Phys. Lett.* **2001**, *78*, 3675.
- [4] O. Tegus, L.-H. Bao, L. Song, *Chin. Phys. B* **2013**, *22*, 037506.
- [5] T. Krenke, E. Duman, M. Acet, E. F. Wassermann, X. Moya, L. Mañosa, A. Planes, *Nat. Mater.* **2005**, *4*, 450.
- [6] a) V. V. Khovaylo, V. V. Rodionova, S. N. Shevyrtalov, V. Novosad, *Phys. Status Solidi B* **2014**, *251*, 2104; b) A. Ludwig, R. Zarnetta, S. Hamann, A. Savan, S. Thienhaus, *Int. J. Mater. Res.* **2008**, *99*, 1144.
- [7] S. Kaufmann, U. K. Rössler, O. Heczko, M. Wuttig, J. Buschbeck, L. Schultz, S. Fähler, *Phys. Rev. Lett.* **2010**, *104*, 145702.
- [8] A. Auge, N. Teichert, M. Meinert, G. Reiss, A. Hütten, E. Yüzüak, I. Dincer, Y. Elerman, I. Ennen, P. Schattschneider, *Phys. Rev. B* **2012**, *85*, 214118.
- [9] B. Dutta, I. Opahle, T. Hickel, *Funct. Mater. Lett.* **2016**, *09*, 1642010.
- [10] B. Dutta, T. Hickel, J. Neugebauer, C. Behler, S. Fähler, A. Behler, A. Waske, N. Teichert, J.-M. Schmalhorst, A. Hütten, *Phys. Status Solidi RRL* **2015**, *9*, 321.
- [11] V. D. Buchelnikov, V. V. Sokolovskiy, H. C. Herper, H. Ebert, M. E. Gruner, S. V. Taskaev, V. V. Khovaylo, A. Hucht, A. Dannenberg, M. Ogura, H. Akai, M. Acet, P. Entel, *Phys. Rev. B* **2010**, *81*, 094411.
- [12] T. Graf, C. Felser, S. S. P. Parkin, *Prog. Solid State Chem.* **2011**, *39*, 1.
- [13] A. Planes, L. Mañosa, M. Acet, *J. Phys. Condens. Matter* **2009**, *21*, 233201.
- [14] V. Srivastava, X. Chen, R. D. James, *Appl. Phys. Lett.* **2010**, *97*, 014101.
- [15] R. Kainuma, Y. Imano, W. Ito, Y. Sutou, H. Morito, S. Okamoto, O. Kitakami, K. Oikawa, A. Fujita, T. Kanomata, K. Ishida, *Nature* **2006**, *439*, 957.
- [16] D. Y. Cong, S. Roth, L. Schultz, *Acta Mater.* **2012**, *60*, 5335.
- [17] S. Fabbri, J. Kamarad, Z. Arnold, F. Casoli, A. Paoluzi, F. Bolzoni, R. Cabassi, M. Solzi, G. Porcari, C. Pernechele, *Acta Mater.* **2011**, *59*, 412.
- [18] R. Kainuma, W. Ito, R. Y. Umetsu, K. Oikawa, K. Ishida, *Appl. Phys. Lett.* **2008**, *93*, 091906.
- [19] Y. Kim, W. B. Han, H.-S. Kim, H. H. An, C. S. Yoon, *J. Alloys Compd.* **2013**, *557*, 265.
- [20] L. Mañosa, A. Planes, M. Acet, E. Duman, E. F. Wassermann, *J. Magn. Magn. Mater.* **2004**, *272–276*, 2090.
- [21] a) R. Kainuma, K. Ishida, H. Nakano, *Metall. Mater. Trans. A* **1996**, *27*, 4153; b) S. Morito, T. Kakeshita, K. Hirata, K. Otsuka, *Acta Mater.* **1998**, *46*, 5377.
- [22] G. Kresse, J. Furthmüller, *Phys. Rev. B* **1996**, *54*, 11169.
- [23] P. E. Blöchl, *Phys. Rev. B* **1994**, *50*, 17953.
- [24] J. P. Perdew, K. Burke, M. Ernzerhof, *Phys. Rev. Lett.* **1996**, *77*, 3865.
- [25] T. Hickel, B. Grabowski, F. Körmann, J. Neugebauer, *J. Phys. Condens. Matter* **2012**, *24*, 053202.
- [26] M. A. Uijttewaal, T. Hickel, J. Neugebauer, M. E. Gruner, P. Entel, *Phys. Rev. Lett.* **2009**, *102*, 035702.
- [27] J. Enkovaara, A. Ayuela, J. Jalkanen, L. Nordström, R. M. Nieminen, *Phys. Rev. B* **2003**, *67*, 054417.
- [28] B. Dutta, T. Hickel, P. Entel, J. Neugebauer, *J. Phase Equilib. Diffus.* **2014**, *35*, 695.
- [29] S. Singh, B. Dutta, S. W. D'Souza, M. G. Zavareh, P. Devi, A. S. Gibbs, T. Hickel, S. Chadov, C. Felser, D. Pandey, *Nat. Commun.* **2017**, *8*, 1006.
- [30] F. Körmann, B. Grabowski, B. Dutta, T. Hickel, L. Mauger, B. Fultz, J. Neugebauer, *Phys. Rev. Lett.* **2014**, *113*, 165503.
- [31] Y. Ikeda, F. Körmann, B. Dutta, A. Carreras, A. Seko, J. Neugebauer, I. Tanaka, in print, <http://arxiv.org/pdf/1702.02389v1>.

- [32] I. Stockem, A. Bergman, A. Glensk, T. Hickel, F. Körmann, B. Grabowski, J. Neugebauer, B. Alling, in print, <http://arxiv.org/pdf/1802.02934v1>.
- [33] F. Körmann, A. Dick, B. Grabowski, T. Hickel, J. Neugebauer, *Phys. Rev. B* **2012**, *85*, 125104.
- [34] J. Neuhaus, W. Petry, A. Krimmel, *Phys. B* **1997**, *234–236*, 897.
- [35] J. Neuhaus, M. Leitner, K. Nicolaus, W. Petry, B. Hennion, A. Hiess, *Phys. Rev. B* **2014**, *89*, 184302.
- [36] B. Alling, F. Körmann, B. Grabowski, A. Glensk, I. A. Abrikosov, J. Neugebauer, *Phys. Rev. B* **2016**, *93*, 224411.
- [37] B. Dutta, A. Çakır, C. Giacobbe, A. Al-Zubi, T. Hickel, M. Acet, J. Neugebauer, *Phys. Rev. Lett.* **2016**, *116*, 025503.
- [38] T. Hickel, M. Uijtewaal, A. Al-Zubi, B. Dutta, B. Grabowski, J. Neugebauer, *Adv. Eng. Mater.* **2012**, *14*, 547.
- [39] A. Çakır, L. Righi, F. Albertini, M. Acet, M. Farle, S. Aktürk, *J. Appl. Phys.* **2013**, *114*, 183912.
- [40] Z. Li, K. Xu, Y. Zhang, C. Tao, D. Zheng, C. Jing, *Sci. Rep.* **2015**, *5*, 15143.
- [41] B. Weise, B. Dutta, N. Teichert, A. Hütten, T. Hickel, A. Waske, *Sci. Rep.* **2018**, *8*, 9147.
- [42] H. C. Xuan, Y. Q. Zhang, H. Li, P. D. Han, D. H. Wang, Y. W. Du, *Appl. Phys. A* **2015**, *119*, 597.
- [43] N. Teichert, D. Kucza, O. Yildirim, E. Yuzuak, I. Dincer, A. Behler, B. Weise, L. Helmich, A. Boehnke, S. Klimova, A. Waske, Y. Elerman, A. Hütten, *Phys. Rev. B* **2015**, *91*, 184405.
- [44] B. Dutta, F. Körmann, T. Hickel, J. Neugebauer, *Phys. Status Solidi B* **2018**, *255*, 1700455.
- [45] K. Ullakko, J. K. Huang, C. Kantner, R. C. O'Handley, V. V. Kokorin, *Appl. Phys. Lett.* **1996**, *69*, 1966.
- [46] a) J.-L. Jin, X.-Q. Zhang, G.-K. Li, Z.-H. Cheng, L. Zheng, Y. Lu, *Phys. Rev. B* **2011**, *83*, 184431; b) M. Fries, K. P. Skokov, D. Y. Karpenkov, V. Franco, S. Ener, O. Gutfleisch, *Appl. Phys. Lett.* **2016**, *109*, 232406.
- [47] L. Caron, B. Dutta, P. Devi, M. Ghorbani Zavareh, T. Hickel, R. Cabassi, F. Bolzoni, S. Fabbri, F. Albertini, C. Felser, S. Singh, *Phys. Rev. B* **2017**, *96*, 054105.
- [48] a) P. Bruno, *Phys. Rev. B* **1989**, *39*, 865; b) G. H. O. Daalderop, P. J. Kelly, M. F. H. Schuurmans, *Phys. Rev. B* **1991**, *44*, 12054.
- [49] a) M. Wagemaker, F. M. Mulder, A. van der Ven, *Adv. Mater.* **2009**, *21*, 2703; b) J. Yoon, S. Jo, I. S. Chun, I. Jung, H.-S. Kim, M. Meitl, E. Menard, X. Li, J. J. Coleman, U. Paik, J. A. Rogers, *Nature* **2010**, *465*, 329.
- [50] a) T. Mukherjee, S. Sahoo, R. Skomski, D. J. Sellmyer, C. Binek, *Phys. Rev. B* **2009**, *79*, 144406; b) Q. Zhang, S. Thota, F. Guillou, P. Padhan, V. Hardy, A. Wahl, W. Prellier, *J. Phys. Condens. Matter* **2011**, *23*, 052201.
- [51] a) R. Caballero-Flores, V. Franco, A. Conde, K. E. Knippling, M. A. Willard, *Appl. Phys. Lett.* **2011**, *98*, 102505; b) V. Franco, A. Conde, *Scripta Mater.* **2012**, *67*, 594; c) M. Krautz, J. Hosko, K. Skokov, P. Svec, M. Stoica, L. Schultz, J. Eckert, O. Gutfleisch, A. Waske, *Phys. Status Solidi C* **2014**, *11*, 1039.
- [52] M. Pasquale, C. P. Sasso, L. H. Lewis, L. Giudici, T. Lograsso, D. Schlagel, *Phys. Rev. B* **2005**, *72*, 094435.
- [53] a) X. Zhang, B. Zhang, S. Yu, Z. Liu, W. Xu, G. Liu, J. Chen, Z. Cao, G. Wu, *Phys. Rev. B* **2007**, *76*, 132403; b) K. Szalowski, T. Balcerzak, *J. Phys. Condens. Matter* **2014**, *26*, 386003; c) S. Fabbri, F. Albertini, A. Paoluzi, F. Bolzoni, R. Cabassi, M. Solzi, L. Righi, G. Calestani, *Appl. Phys. Lett.* **2009**, *95*, 022508.
- [54] H. Zhang, Y. J. Sun, L. H. Yang, E. Niu, H. S. Wang, F. X. Hu, J. R. Sun, B. G. Shen, *J. Appl. Phys.* **2014**, *115*, 063901.
- [55] R. Barua, B. T. Lejeune, L. Ke, G. Hadjipanayis, E. M. Levin, R. W. McCallum, M. J. Kramer, L. H. Lewis, *J. Alloy. Compd.* **2018**, *745*, 505–512.
- [56] a) A. Fujita, S. Fujieda, K. Fukamichi, H. Mitamura, T. Goto, *Phys. Rev. B* **2001**, *65*, 014410; b) E. Brück, J. Kamarad, V. Sechovsky, Z. Arnold, O. Tegus, F. R. de Boer, *J. Magn. Magn. Mater.* **2007**, *310*, e1008–e1009; c) J. Liu, T. Gottschall, K. P. Skokov, J. D. Moore, O. Gutfleisch, *Nat. Mater.* **2012**, *11*, 620.
- [57] T. Gottschall, D. Benke, M. Fries, A. Taubel, I. A. Radulov, K. P. Skokov, O. Gutfleisch, *Adv. Funct. Mater.* **2017**, *27*, 1606735.
- [58] T. Gottschall, K. P. Skokov, D. Benke, M. E. Gruner, O. Gutfleisch, *Phys. Rev. B* **2016**, *93*, 184431.
- [59] L. Jia, J. R. Sun, B. G. Shen, D. X. Li, S. Nimori, *J. Appl. Phys.* **2007**, *101*, 106108.
- [60] A. Fujita, K. Fukamichi, M. Yamada, T. Goto, *J. Appl. Phys.* **2003**, *93*, 7263.
- [61] J. Lyubina, *J. Appl. Phys.* **2011**, *109*, 07A902.
- [62] J. Lyubina, K. Nenkov, L. Schultz, O. Gutfleisch, *Phys. Rev. Lett.* **2008**, *101*, 177203.
- [63] Z. Gercsi, N. Fuller, K. G. Sandeman, A. Fujita, *J. Phys. D* **2018**, *51*, 034003.
- [64] M. Krautz, K. Skokov, T. Gottschall, C. S. Teixeira, A. Waske, J. Liu, L. Schultz, O. Gutfleisch, *J. Alloys Compd.* **2014**, *598*, 27.
- [65] K. Fukamichi, A. Fujita, S. Fujieda, *J. Alloys Compd.* **2006**, *408–412*, 307.
- [66] A. Fujita, H. Yako, *Scripta Mater.* **2012**, *67*, 578.
- [67] C. Salazar Mejía, R. Kuchler, A. K. Nayak, C. Felser, M. Nicklas, *Appl. Phys. Lett.* **2017**, *110*, 071901.
- [68] M. Wodniok, N. Teichert, L. Helmich, A. Hütten, *AIP Adv.* **2017**, *7*, 056428.
- [69] M. G. Loving, R. Barua, C. Le Graët, C. J. Kinane, D. Heiman, S. Langridge, C. H. Marrows, L. H. Lewis, *J. Phys. D* **2018**, *51*, 024003.
- [70] A. Fujita, Y. Akamatsu, K. Fukamichi, *J. Appl. Phys.* **1999**, *85*, 4756.
- [71] A. Waske, L. Giebeler, B. Weise, A. Funk, M. Hinterstein, M. Herklotz, K. Skokov, S. Fähler, O. Gutfleisch, J. Eckert, *Phys. Status Solidi RRL* **2015**, *9*, 136.
- [72] C. Bennati, F. Laviano, G. Durin, E. S. Olivetti, V. Basso, G. Ghigo, M. Kuepferling, *J. Magn. Magn. Mater.* **2016**, *400*, 339.
- [73] R. I. Niemann, Dissertation, Technische Universität Dresden, **2015**.
- [74] H. Neves Bez, K. K. Nielsen, A. Smith, P. Norby, K. Ståhl, C. R. H. Bahl, *Appl. Phys. Lett.* **2016**, *109*, 051902.
- [75] a) R. Das, A. Perumal, A. Srinivasan, *J. Alloys Compd.* **2013**, *572*, 192; b) J. Huang, N. Sun, C. Liu, Y. Ge, T. Zhang, F. Liu, P. Si, *Acta Metall. Sin. (Engl. Lett.)* **2014**, *27*, 27.
- [76] R. Wu, F. Shen, F. Hu, J. Wang, L. Bao, L. Zhang, Y. Liu, Y. Zhao, F. Liang, W. Zuo, J. Sun, B. Shen, *Sci. Rep.* **2016**, *6*, 20993.
- [77] J. J. Ipus, J. M. Borrego, L. M. Moreno-Ramírez, J. S. Blázquez, V. Franco, A. Conde, *Intermetallics* **2017**, *84*, 30.
- [78] R. Niemann, S. Hahn, A. Diestel, A. Backen, L. Schultz, K. Nielsch, M. F.-X. Wagner, S. Fähler, *APL Mater.* **2016**, *4*, 064101.
- [79] R. Niemann, J. Baró, O. Heczko, L. Schultz, S. Fähler, E. Vives, L. Mañosa, A. Planes, *Phys. Rev. B* **2012**, *86*, 214101.
- [80] H. E. Karaca, I. Karaman, B. Basaran, D. C. Lagoudas, Y. I. Chumlyakov, H. J. Maier, *Acta Mater.* **2007**, *55*, 4253.
- [81] D. Tabor, *Br. J. Appl. Phys.* **1956**, *7*, 159.
- [82] A. Waske, E. Lovell, A. Funk, K. Sellschopp, A. Rack, L. Giebeler, P. F. Gostin, S. Fähler, L. F. Cohen, *APL Mater.* **2016**, *4*, 106101.
- [83] A. M. Tishin, Y. I. Spichkin, *The Magnetocaloric Effect and Its Applications*, Institute of Physics, Bristol, **2003**.
- [84] H. Yako, S. Fujieda, A. Fujita, K. Fukamichi, *IEEE Trans. Magn.* **2011**, *47*, 2482.
- [85] P. Ranzieri, S. Fabbri, L. Nasi, L. Righi, F. Casoli, V. A. Chernenko, E. Villa, F. Albertini, *Acta Mater.* **2013**, *61*, 263.
- [86] S. Kaufmann, R. Niemann, T. Thersleff, U. K. Röbber, O. Heczko, J. Buschbeck, B. Holzapfel, L. Schultz, S. Fähler, *New J. Phys.* **2011**, *13*, 053029.
- [87] N. Teichert, A. Auge, E. Yüzüak, I. Dincer, Y. Elerman, B. Krumme, H. Wende, O. Yildirim, K. Potzger, A. Hütten, *Acta Mater.* **2015**, *86*, 279.
- [88] R. Niemann, A. Backen, S. Kauffmann-Weiss, C. Behler, U. K. Röbber, H. Seiner, O. Heczko, K. Nielsch, L. Schultz, S. Fähler, *Acta Mater.* **2017**, *132*, 327.
- [89] A. Diestel, A. Backen, V. Neu, L. Schultz, S. Fähler, *Scripta Mater.* **2012**, *67*, 423.
- [90] N. Teichert, Dissertation, Universität Bielefeld, **2016**.
- [91] K. G. Sandeman, *Scripta Mater.* **2012**, *67*, 566.
- [92] B. D. Cullity, C. D. Graham, *Introduction to Magnetic Materials, Second Edition*, Wiley, Hoboken, **2008**.
- [93] J. M. D. Coey, *Magnetism and Magnetic Materials*, Cambridge University Press, Cambridge, **2010**.

- [94] B. Schwarz, N. Mattern, J. D. Moore, K. P. Skokov, O. Gutfleisch, J. Eckert, *J. Magn. Magn. Mater.* **2011**, 323, 1782.
- [95] R. Bjørk, C. R. H. Bahl, *Appl. Phys. Lett.* **2013**, 103, 102403.
- [96] E. Lovell, A. M. Pereira, A. D. Caplin, J. Lyubina, L. F. Cohen, *Adv. Energy Mater.* **2015**, 5, 1401639.
- [97] A. Fujita, T. Kondo, M. Kano, H. Yako, *Appl. Phys. Lett.* **2013**, 102, 041913.
- [98] E. Lovell, M. Bratko, A. D. Caplin, A. Barcza, M. Katter, L. Ghivelder, L. F. Cohen, *Philos. Trans. R. Soc. London Ser. A* **2016**, 374, 20150307.
- [99] L. F. Cohen, *Phys. Status Solidi B* **2018**, 255, 1700317.
- [100] A. Funk, M. Zeilinger, F. Dötz, I. Soldatov, R. Schäfer, A. Waske, *Phys. Status Solidi B* **2018**, 255, 1700345.
- [101] I. A. Radulov, K. P. Skokov, D. Y. Karpenkov, T. Gottschall, O. Gutfleisch, *J. Magn. Magn. Mater.* **2015**, 396, 228.
- [102] M. Földeàki, R. Chahine, T. K. Bose, *J. Appl. Phys.* **1995**, 77, 3528.

Manuscript received: February 28, 2018
Revised manuscript received: May 8, 2018
Accepted manuscript online: May 10, 2018
Version of record online: August 5, 2018